Draft version October 28, 2009
Preprint typeset using LaTeX style emulateapj v. 04/20/08

FORMATION OF TORUS-UNSTABLE FLUX ROPES AND ELECTRIC CURRENTS IN ERUPTING SIGMOIDS

G. Aulanier, T. Török and P. Démoulin
LESIA, Observatoire de Paris, CNRS, UPMC, Université Paris Diderot, 5 place Jules Janssen, 92190 Meudon, France

E. E. DeLuca
Harvard-Smithsonian Center for Astrophysics, 60 Garden Street, Cambridge, MA 02139, USA
Draft version October 28, 2009

ABSTRACT

We analyze the physical mechanisms that form a three-dimensional coronal flux rope and later cause its eruption. This is achieved by a zero-β MHD simulation of an initially potential, asymmetric bipolar field, which evolves by means of simultaneous slow magnetic field diffusion and sub-Alfvénic, line-tied shearing motions in the photosphere. As in similar models, flux-cancellation driven photospheric reconnection in a bald-patch separatrix transforms the sheared arcades into a slowly rising and stable flux rope. A bifurcation from a bald-patch to a quasi-separatrix layer (QSL) topology occurs later on in the evolution, while the flux rope keeps growing and slowly rising, now due to shear-driven coronal slip-running reconnection, which is of tether-cutting type and takes place in the QSL. As the flux rope reaches the altitude at which the decay index $-\partial \ln B/\partial \ln z$ of the potential field exceeds $\sim 3/2$, it rapidly accelerates upward while the overlying arcade eventually develops an inverse tear-drop shape, as observed in coronal mass ejections (CMEs). This transition to eruption is in accordance with the onset criterion of the torus instability. Thus we find that photospheric flux-cancellation and tether-cutting coronal reconnection do not trigger CMEs in bipolar magnetic fields, but are key pre-eruptive mechanisms for flux ropes to build up and to rise to the critical height above the photosphere at which the torus instability causes the eruption. In order to interpret recent *Hinode X-Ray Telescope* observations of an erupting sigmoid, we produce simplified synthetic soft X-ray images from the distribution of the electric currents in the simulation. We find that a bright sigmoidal envelope is formed by pairs of J-shaped field lines in the pre-eruptive stage. These field lines form through the bald-patch reconnection, and merge later on into S-shaped loops through the tether-cutting reconnection. During the eruption, the central part of the sigmoid brightens due to the formation of a vertical current layer in the wake of the erupting flux rope. Slip-running reconnection in this layer yields the formation of flare loops. A rapid decrease of currents due to field line expansion, together with the increase of narrow currents in the reconnecting QSL, yields the sigmoid hooks to thin in the early stages of the eruption. Finally, a slightly rotating erupting loop-like feature (ELLF) detaches from the center of the sigmoid. Most of this ELLF is not associated with the erupting flux rope, but with a current shell which develops within expanding field lines above the rope. Only the short, curved end of the ELLF corresponds to a part of the flux rope. We argue that the features found in the simulation are generic for the formation and eruption of soft X-ray sigmoids.

Subject headings: MHD - Sun: coronal mass ejections - Sun: magnetic fields - Sun: X-rays

1. INTRODUCTION

1.1. *Solar eruptions*

Coronal mass ejections (CMEs) are large clouds of magnetized plasma, which are ejected from the solar atmosphere into interplanetary space. They are formed by the eruption of low-altitude coronal loops, predominantly located within active regions. CMEs are frequently accompanied by a flare, and by the eruption of one or several of the following features: a prominence, a soft X-ray sigmoid, trans-equatorial or active region interconnecting loops. These solar eruptions typically start with an initiation phase, sometimes observable by the slow rise of a loop and/or a filament, and increasing pre-flare emission in EUV and X-rays. This phase is followed by the eruption itself, during which the system accelerates up to typical velocities of $100-1000$ km/s (although slower and faster CMEs also exist) while flare loops almost always form in the wake of the eruption. After the acceleration phase, the resulting CME propagates with an approximately constant velocity (until it enters the heliosphere where it interacts with the solar wind). The rapid acceleration is typically correlated with the impulsive flare energy release, and with the transient brightening of a soft X-ray sigmoid, if one is present before the eruption. These well-defined phases and phenomena (as reviewed by, e.g. Forbes 2000; van Driel-Gesztelyi et al. 2000; Vršnak 2008) suggest that distinct mechanisms might be at work during the initiation and the rapid acceleration of solar eruptions.

Since the corona is a sufficiently collisional plasma, its evolution can be studied in the frame of the MHD theory. Except during CMEs and flares, the plasma β (the ratio between thermal and magnetic pressure) is very small in the low solar corona, $\beta \ll 1$. Therefore, the magnetic energy dominates all other forms of energy in the source regions of solar eruptions (see Forbes 2000, Table 2). Current-free (potential) magnetic fields cor-

respond to the minimum magnetic energy for a given distribution of magnetic flux through the dense photosphere. Since the photospheric flux distribution does not significantly change during the time-scales of eruptions, and since the powering of eruptions requires the magnetic energy to decrease, the coronal magnetic field must therefore be highly non-potential prior to eruption onset, i.e. it must contain strong electric current densities. Due to the slow evolution of the photospheric magnetic field (as compared to typical coronal velocities), currents which are injected into the corona must accumulate slowly, such that the coronal field evolves quasi-statically, as a sequence of force-free equilibria. The triggering of CMEs therefore requires the coronal field to reach some threshold above which the balance between magnetic pressure (which points upward) and magnetic tension (which points downward) is broken. When the systems suddenly enters a regime in which the pressure dominates, it can erupt in a catastrophic way, leading to a CME. The resulting ideal expansion of the magnetic field, as well as the resistively driven magnetic reconnection in the current layer that forms in the wake of the expanding system, both contribute to decrease the magnetic energy. These arguments are the root of the "storage-and-release" MHD models for solar eruptions.

Even though it is now widely accepted that solar eruptions are due to such a violent destabilization of previously energized coronal magnetic fields, the detailed mechanisms which bring a system into an eruptive stage, and which eventually drive the eruption, are not yet fully understood. A large variety of storage-and-release models has been put forward in the past decades (see Forbes et al. 2006, for an extensive review, that also describes other classes of models). These models often have common features and are able to describe many individual observed aspects of solar eruptions. It is therefore not always clear which of the suggested mechanisms can account for both the slow initiation and for the rapid acceleration of the ejecta. One aim of this paper is to test some of the proposed mechanisms with respect to this question.

1.2. *Circuit and MHD non-equilibrium models*

The seminal eruption model is the 2.5D cartesian circuit model (van Tend & Kuperus 1978; van Tend 1979; Molodenskii & Filippov 1987; Filippov & Den 2001). In this model, a line current I is inserted at some height $z = h$ above the photospheric plane, $z = 0$, into an ambient coronal field $B_{\rm ex}$, and a so-called "image current" $-I$ is added at $z = -h$ to emulate one effect of photospheric line tying, namely that the current induced magnetic field cannot pass through the photosphere. The resulting coronal magnetic field consists of a detached plasmoid (or flux rope) embedded in a coronal arcade, with the rope axis located at $z = h$. In the "circuit point of view", the equilibrium of the system results from the competition between two Laplace forces, namely the downward force that $B_{\rm ex}$ excerts on the coronal line current, and the upward force generated by the repulsion of the two line currents. In the "MHD point of view", the former corresponds to restraining magnetic tension of the potential field overlying the flux rope, and the latter to magnetic pressure that results from the increase of the magnetic field strength below the coronal line current induced by the photospheric boundary. In this model, the equilibrium curve $h(I)$ has a critical point $(I_c; h_c)$, beyond which the line-current $I \geq I_c$ cannot stay in equilibrium and must move to infinite z. The altitude $z = h_c$ of this critical point is given by the height at which $B_{\rm ex}(z)$ starts to drop faster than z^{-1}.

The model has been refined several times, e.g. by including a coronal current of finite width and photospheric line tying of the arcades surrounding the flux rope. The latter yields the formation of a vertical current sheet below the flux rope during its eruption (Martens & Kuin 1989; Forbes & Isenberg 1991). This current sheet exerts an extra restraining force on the line current, such that the flux rope cannot move to infinity, but finds a new equilibrium position at finite z. A full eruption therefore requires the dissipation of these developing currents by sufficiently fast magnetic reconnection (e.g. Lin & Forbes 2000). The resulting "non-equilibrium" has been found to account for eruptions of 2.5D flux ropes in line-tied MHD simulations (Forbes 1990).

The model has also been investigated in 2.5D axisymmetric (toroidal) geometry. In a first approach, the coronal line-current is replaced by a detached ring-current at some height above the photospheric spherical surface. If an image current is added below the photosphere and if line-tying of the coronal arcades surrounding the flux rope is taken into account, the same repulsive and restraining forces as discussed above contribute to the force balance. However, a new repulsive force (which the current exerts on itself due to its bending) comes into play. This curvature (or "hoop") force is radially outward directed and can be balanced by an external magnetic field, $B_{\rm ex}$ (Shafranov 1966; Chen 1989; Titov & Démoulin 1999). The dependance of the non-equilibrium of the ring-current to the magnitude of $B_{\rm ex}$ has been analyzed by Lin et al. (1998). In a second approach, half of the ring-current of radius R is placed above a reference (photospheric) plane, and the other half located below somehow plays the role of the image current. In the absence of any line-tying, the ring-current can freely expand radially, as a result of the so-called "torus instability". This instability occurs when the restoring force due to $B_{\rm ex}$ drops faster with R than the hoop force. For external poloidal fields (i.e. perpendicular to the current) with $B_{\rm ex} \sim R^{-n}$, the instability threshold is given by $n_c \sim 3/2$ (Bateman 1978; Kliem & Török 2006).

Even if the line-tying of the coronal arcades has been treated, the absence of line-tying of the flux rope ends in these models has raised questions on their validity for solar eruptions. Only very recently, this important effect has been calculated analytically by Isenberg & Forbes (2007), through the addition of multiple image current segments. Also, it has been shown that the torus instability can drive eruptions also in fully 3D line-tied MHD simulations (Török & Kliem 2007; Fan & Gibson 2007): both found instability thresholds very similar to that of a freely expanding ring-current. Retrospectively, this same instability may also have triggered the eruption in past line-tied MHD simulations (Roussev et al. 2003; Török & Kliem 2005) which used initial conditions based on the Titov & Démoulin (1999) model, as in Török & Kliem (2007).

An important missing element of the circuit models, however, is the consistent treatment of the pre-eruptive

evolution, and therefore the identification of the physical mechanisms that allow the ratios I/I_c and h/h_c to evolve from < 1 during the long-lasting energy storage period toward > 1, for which an eruption can suddenly occur. Several models have been proposed to achieve this goal. We describe and classify them hereafter, even though classification is not straightforward since several of these models incorporate common features.

1.3. *MHD models based on current increase*

Slow line-tied photospheric footpoint shearing motions of initially potential fields do induce field-aligned coronal currents (e.g. Low 1977; Yang et al. 1986). However, the resulting expansion of the system increases the length of the field lines, which in turn tends to reduce the induced currents. Analytical arguments (Aly 1985; Klimchuk & Sturrock 1989; Sturrock et al. 1995) and numerical simulations (Mikic & Linker 1994; Roumeliotis et al. 1994; Amari et al. 1996a; Aulanier et al. 2005a) have shown that, in ideal MHD, the expansion-driven current decrease eventually dominates the shear-driven current increase, which does not allow the magnetic field to reach any loss of equilibrium. This suggests that simple line-tied shearing/twisting motions are not sufficient to trigger an eruption (although, see Török & Kliem 2003; Rachmeler et al. 2009).

The electric current in the corona could also be directly amplified by the emergence of strongly twisted flux ropes from the convection zone (Emonet & Moreno-Insertis 1998; Jouve & Brun 2009) through the photosphere. "Kinematic flux emergence" models, in which the emergence is prescribed as time-dependent boundary conditions for the magnetic field in a line-tied photospheric boundary, indeed lead to eruptions (Fan & Gibson 2004; Amari et al. 2004). Such eruptions have been attributed to the torus instability (Fan & Gibson 2007).

Although most eruptions do not occur in the early stages of active region evolution (e.g. Démoulin et al. 2002), this mechanism may explain some CMEs, but it requires further study: Non-kinematic flux emergence simulations show that, due to the weight of photospheric plasma which is trapped in dips of the flux rope, its axis hardly emerges (Fan 2001; Magara & Longcope 2001; Archontis et al. 2004), whereas this appears to be necessary to drive an eruption in kinematic models. If the flux rope is not strongly curved, the only way for the lower part of the flux rope to emerge is to dispose of the dense plasma trapped in its windings. According to the "resistive flux emergence model" this may take place through magnetic reconnection photospheric U-loops (e.g. Pariat et al. 2004; Amari et al. 2005; Isobe et al. 2007).

1.4. *MHD models based on tension reduction*

Instead of increasing the current to a value $I \geq I_c$ for a given external magnetic field $B_{\rm ex}$, an alternative approach is to reduce the restraining tension of coronal arcades which overlie initially stable current-carrying magnetic fields. Most eruption models actually fall into this class.

The first possibility is the breakdown of ideal MHD in the vertical current-sheet that forms within a shearing arcade (Amari & Aly 1990), resulting in tether-cutting reconnection in the corona (Sturrock 1989; Moore & Roumeliotis 1992; Moore et al. 2001). This non-ideal effect creates and feeds a current-carrying flux rope from the flux of the arcades, thus reducing their downward tension. This effects has indeed been shown to trigger eruptions in 2.5D cartesian (Amari et al. 1996a) and axisymmetric (Mikic & Linker 1994; Jacobs et al. 2006) MHD simulations, as soon as non-ideal effects are included. However, even though tether-cutting reconnection has been found to sustain the formation of twisted field lines in 3D MHD simulations of sheared non-eruptive fields (DeVore & Antiochos 2000), and of emerging erupting fields (Manchester et al. 2004; Archontis & Török 2008), it has so far not been identified to be a main eruption driver in any 3D MHD simulations.

A second possibility is to remove the overlying arcades by coronal reconnection, e.g. in a coronal magnetic nullpoint (Antiochos et al. 1999). This "breakout" mechanism has been found to work in MHD simulations, both in 2.5D (e.g. MacNeice et al. 2004; van der Holst et al. 2007) and in 3D (e.g. Lynch et al. 2008). Other models also explain eruptions by the lowering of the magnetic tension through coronal null point reconnection, but in those the reconnection takes place aside of the current-carrying flux tube (Chen & Shibata 2000; Lin et al. 2001; Jacobs et al. 2009) instead of above it. Still, such models cannot account for all CMEs, since they require the existence of a multi-polar configuration (which not always present, see, e.g. Démoulin et al. 2002), as well as the pre-eruptive activation of the nullpoint (which is not always observed, see, e.g. Li et al. 2006; Ugarte-Urra et al. 2007).

A third way is to reduce the length-scales of the whole photospheric magnetic bipole in which the overlying arcades are rooted. This leads to a faster decrease of the magnetic field with height, and therefore facilitates the development of non-equilibrium of twisted force-free flux ropes (Forbes & Priest 1995; Török & Kliem 2007). Eruptions of current-carrying fields subject to converging motions have been found in both 2.5D (Inhester et al. 1992) and 3D (e.g. Amari et al. 2003a) MHD simulations.

A fourth class of models, sometimes referred to as "flux cancellation", but in reality based on the "disappearance of magnetic flux", is also able to produce eruptions of pre-existing detached flux ropes (in axisymmetric geometry, see Lin et al. 1998), as well as the formation and subsequent eruption of anchored flux ropes (in 3D cartesian geometry, see Amari et al. 2000; Lin et al. 2002). These models rely on an ad-hoc homogeneous magnetic field decrease all over the photosphere, which is imposed either by reducing the magnetic momentum of the external subphotospheric magnetic field sources, or by prescribing adequate horizontal electric fields in the photosphere. The disappearance of flux yields a diminution of the magnetic energy of the open field to a value which is below that of the whole magnetic field, thus triggering an eruption (Amari et al. 2000). The physical validity of these models, however, has yet to be established. A significant decrease of magnetic field amplitudes over large areas preceding a CME has been observed (Schmieder et al. 2008), but such a decrease can also support the model described in the following.

1.5. *Flux cancellation model*

The "flux-dispersal" model for solar eruptions incorporates several features of the models described above. It is based on the observed evolution of magnetic flux concentrations in the photosphere, e.g. within or between bipolar active regions (e.g. Démoulin et al. 2002; van Driel-Gesztelyi et al. 2003). Over time periods of weeks or months, flux concentrations disperse in all directions, and their total magnetic flux slowly and weakly decreases through local flux convergence and cancellation at polarity inversion lines (hereafter PIL). In that respect, observationnally speaking and unlike the flux disappearance model, the flux dispersal model is a "flux-cancellation" model, so this is how we refer to it in this paper.

Flux convergence and cancellation have been shown to yield the formation of a flux rope through tether-cutting-like photospheric reconnection between previously sheared arcades in a 2.5D geometry (van Ballegooijen & Martens 1989). This process forms a "bald-patch" in the PIL, along which magnetic field lines are curved upwards and are tangent to the photosphere (Titov et al. 1993). Converging motions and flux cancellation at the PIL (without flux dispersal or decrease) have been found to trigger eruptions in 2.5D circuit models (Forbes & Isenberg 1991; Isenberg et al. 1993). Flux ropes have been also found to form and erupt in fully 3D line-tied MHD simulations, if the large-scale decay of a symmetric photospheric magnetic field is modeled by a homogeneous photospheric diffusion term that applies to the vertical component of the magnetic field in the induction equation (Amari et al. 2003b; Mackay & van Ballegooijen 2006).

1.6. *Aims of this study*

Numerous physical effects take place in 3D MHD flux-cancellation simulations of solar eruptions: current increase through footpoint shearing; flux disappearance through cancellation; tether-cutting; and maybe circuit-type loss of equilibrium. Since they all constitute fundamental mechanisms of several eruption models listed above, the nature of the actual driving mechanism of the eruption (i.e. the mechanism which is responsible for the rapid acceleration of the erupting flux) has never been formally identified in the flux cancellation model.

In this paper, we identify the order in which these effects take place when line-tied shearing footpoint motions and photospheric diffusion occur simultaneously in a system that does not possess artificial symmetries. This investigation justifies the long review of storage-and-release eruption models presented above and allows us to identify the driving mechanism in flux-cancellation models.

Our model settings are described in Sect. 2. The time-evolution of the magnetic field in the pre-eruptive and in the eruptive phase is described in Sect. 3 and Sect. 4, respectively. More specifically, the identification of the eruption driver is achieved in Sect. 4.3. The description of the complex time-sequence of events in the model requires us to briefly illustrate the complex topologies and three-dimensional reconnection regimes which develop during the evolution of the system. A full analysis of these issues is, however, beyond the scope of the present study which focuses on the eruption mechanisms. It will be the object of a future dedicated paper.

In order to test our model against observations, we analyse in Sect. 5 the shapes and dynamics of both magnetic field lines and electric current layers and compare them to fine-scale structures in coronal sigmoids, as observed in soft X-rays before and during their eruption (Manoharan et al. 1996; Rust & Kumar 1996; Sterling & Hudson 1997; Hudson et al. 1998; Sterling et al. 2000; Moore et al. 2001; Canfield et al. 1999; Gibson et al. 2002; Kim et al. 2007). Our asymmetric model settings allow a nearly direct comparison with an erupting sigmoid observed on 2007 February 12 by the *X-Ray Telescope* (*XRT*, see Golub et al. 2007) onboard the *Hinode* satellite (Kosugi et al. 2007). We interpret the wealth of high-resolution soft X-ray features which were reported for this single event by McKenzie & Canfield (2008), and we compare them to previously published MHD interpretations for sigmoids (as reviewed by Green et al. 2007).

2. MHD FLUX-CANCELLATION MODEL

2.1. *Equations and initial conditions*

We model the formation and eruption of a coronal flux rope using the zero-β (pressureless) time-dependent 3D MHD code, which is extensively described in Aulanier et al. (2005a). This code solves the following equations in cartesian coordinates, where z is the altitude and $z = 0$ is the photospheric plane:

$$\frac{\partial \rho}{\partial t} = -\nabla \cdot (\rho \mathbf{u}) + \zeta\, \Delta(\rho - \rho_\circ) \tag{1}$$

$$\rho\, \frac{\partial \mathbf{u}}{\partial t} = -\rho\, (\mathbf{u} \cdot \nabla)\mathbf{u} + \jmath \times \mathbf{B} + \rho\, \nu'\, \mathfrak{D}\mathbf{u} \tag{2}$$

$$\frac{\partial \mathbf{B}}{\partial t} = \nabla \times (\mathbf{u} \times \mathbf{B}) + \eta\, \Delta \mathbf{B} \tag{3}$$

$$\nabla \times \mathbf{B} = \mu \jmath\,. \tag{4}$$

There, ρ is the mass density ($\rho_\circ$ is its initial value at $t = 0$), $\mathbf{u}$ the plasma velocity, $\mathbf{B}$ the magnetic field, $\jmath$ the electric current-density, and η the magnetic resistivity. $\zeta\, \Delta(\rho - \rho_\circ)$ is an artificial diffusion operator for the density, whose inclusion is necessary to smooth the sharp density gradients which develop during the evolution. Its form ensures that only density variations with respect to $t = 0$ are diffused. $\nu' \mathfrak{D}$ is a diffusion operator for the velocity, which has a Laplacian form that applies to mesh units rather than to physical units. This ensures that the pseudo-viscosity ν' acts on the local size of mesh intervals (see Aulanier et al. 2005a, for details). The equations are solved in their fully developed form, suppressing all $\nabla \cdot \mathbf{B}$ terms.

The boundary conditions at $z = 0$ are line-tied (with the addition of a diffusive effect, see Sect. 2.2), those at the five other faces are open, and they are implemented using two layers of ghost cells at each boundary. The simulation is done in a physical domain $x; y \in [-10, 10]$ and $z \in [0, 30]$, using a highly non-uniform mesh with $n_x \times n_y \times n_z = 251 \times 251 \times 231$ points without ghost cells. The mesh intervals vary in the range $dx; dy \in [6 \times 10^{-3}, 0.32]$ and $dz \in [6 \times 10^{-3}, 0.6]$, expanding from $x = y = z = 0$ following $d_x^{i+1}/d_x^i = d_y^{j+1}/d_y^j \simeq 1.032$ and $d_z^{k+1}/d_z^k \simeq 1.02$.

We use an initial current-free (potential) magnetic field $\mathbf{B}(t = 0)$, which results from two unbalanced monopoles placed at a horizontal distance $L = 2$ from each other,

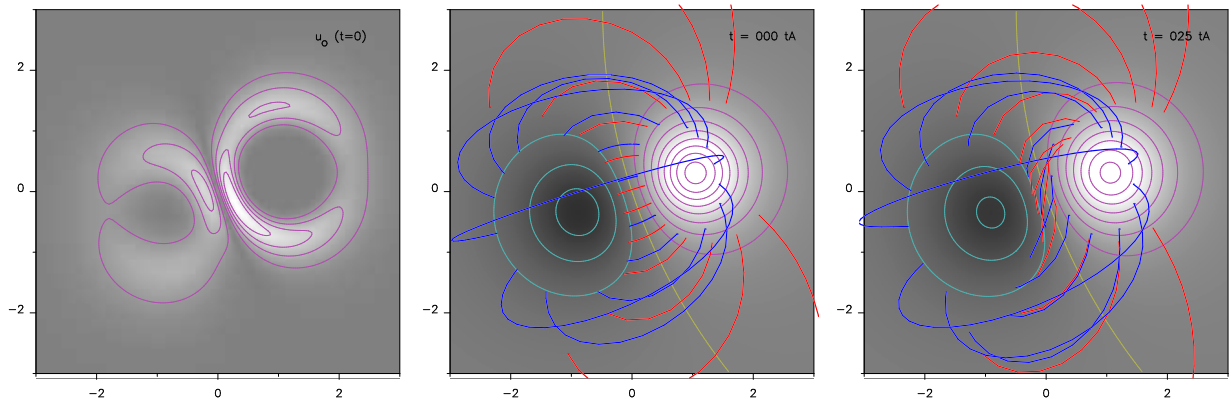

FIG. 1.— [*left:*] Greyscale rendering of the norm of the prescribed photospheric velocity $u_\circ(t=0)$ at $z=0$, outlining the annular shape of the vortices. The pink contours stand for $u_\circ = 0.01; 0.02; 0.03; 0.04$ $c_A(t=0)$. [*middle; right:*] Top view on selected magnetic field lines at $t = 0; 25\ t_A$. The greyscale image shows the vertical photospheric magnetic field component $B_z(z=0)$, where white/black depicts positive/negative B_z. Cyan contours stand for $B_z = 2; 4; 6$, and pink contours for $B_z = 2; 4; 6; 8; 10; 12; 14; 16$. The yellow contour shows the inversion line $B_z = 0$. Red/blue field lines are plotted with fixed footpoints in the negative/positive polarity, chosen such that their conjugate footpoints are located in regions of large velocity within the vortices.

and at different depths $z < 0$. It is given by:

$$B_x(t=0) = \Sigma_{i=1}^{2}\, C_i\,(x-x_i)\,r_i^{-3}\,,$$
$$B_y(t=0) = \Sigma_{i=1}^{2}\, C_i\,(y-y_i)\,r_i^{-3}\,,$$
$$B_z(t=0) = \Sigma_{i=1}^{2}\, C_i\,(z-z_i)\,r_i^{-3}\,,$$
$$r_i = \sqrt{(x-x_i)^2+(y-y_i)^2+(z-z_i)^2}\,, \qquad (5)$$

where $(x_1 = 1.025\,;\, y_1 = 0.3\,;\, z_1 = -0.9\,;\, C_1 = 15)$ and $(x_2 = -0.775\,;\, y_2 = -0.3\,;\, z_2 = -1.3\,;\, C_2 = -14)$. This results in an asymmetric magnetic field configuration, which was motivated by our desire to make a model first that is not potentially biased by artificial symmetries, and second that can be applied to observations of active regions (which typically show a more compact leading polarity). In order to prevent the Alfvén speeds at large z from dropping to values smaller than those prescribed in the photosphere (see Sect. 2.3), which would create undesireable steepening of wavefronts into shocks at high altitudes, we prescribe an arbitrary initial density profile

$$\rho(t=0) = B^2(t=0)\,. \qquad (6)$$

This yields a uniform initial Alfvén speed $c_A(t=0) = 1$ and defines the time unit $t_A = 1$ as the transit time of Alfvén waves over the half-distance, $\approx L/2$, between the centers of the magnetic polarities at $z = 0$.

Within the domain, we fix $\eta = 4.8 \times 10^{-4}$, $\zeta = 1.5\ \eta$ and $\nu' = 25$. At the scale of the smallest mesh interval $d = 6 \times 10^{-3}$ and of the distance $L = 2$, these coefficients result in small characteristic diffusion speeds of $u_\eta^d = 0.08$, $u_\eta^L = 2.4 \times 10^{-4}$, and $u_\zeta = 1.5\ u_\eta$. The pseudo-viscosity leads to a large characteristic diffusion speed $u_{\nu'}^d = 0.15$. This value is unnecessarily large in the pre-eruptive phase, but is required to ensure numerical stability during the eruption (as in Aulanier et al. 2005a). The viscous coefficient had to be doubled for $t > 138\ t_A$ in the present simulation to ensure numerical stability during the development of large plasma velocities (see Sect. 4.1.)

2.2. *Photospheric magnetic flux cancellation*

At a line-tied boundary, the vertical velocity u_z is zero, the horizontal velocities $\mathbf{u}_\perp = (u_x; u_y)$ are prescribed, and the resistivity η is zero by definition. In this paper, we allow a finite and two-dimensional resistivity at the photospheric plane, $\eta(z=0) = \eta^{\rm phot}$. With these settings, Eq. (3) at z=0 turns into:

$$\frac{\partial B_h}{\partial t}(z=0) = \eta^{\rm phot}\,\gamma(t)\,\Delta_\perp B_h - (\mathbf{u}_\perp\cdot\nabla_\perp)B_h - B_h\,(\nabla\cdot\mathbf{u}) + (\mathbf{B}\cdot\nabla)u_h \qquad (7)$$

$$\frac{\partial B_z}{\partial t}(z=0) = \eta^{\rm phot}\,\gamma(t)\,\Delta_\perp B_z - (\mathbf{u}_\perp\cdot\nabla_\perp)B_z - B_z\,(\nabla_\perp\cdot\mathbf{u}_\perp)\,, \qquad (8)$$

where $h = x$ or y, $\nabla_\perp = (\partial/\partial x; \partial/\partial y)$ and $\Delta_\perp = (\partial^2/\partial x^2 + \partial^2/\partial y^2)$. In our code, the boundary conditions for the z derivatives imply that $\partial^2/\partial z^2 = 0$ at $z = 0$, i.e. the equation for the diffusive term is the same at and above $z = 0$. $\gamma(t)$ is a ramp function:

$$\gamma(t) = \frac{1}{2}\,\tanh\left(2\frac{t-t_1}{t_2}\right) + \frac{1}{2}\,, \qquad (9)$$

with $t_1 = 10\ t_A$ and $t_2 = 3\ t_A$, that allows the initial field to reach a numerical equilibrium before the photospheric diffusion starts to take place.

The effect of the term $\eta^{\rm phot}\,\Delta\mathbf{B}$ is to diffuse all three components of the magnetic field in the photosphere. This leads to a horizontal expansion of both magnetic polarities and to a gradual decrease of the field amplitudes at their centers. Around the PIL (defined by the curve $B_z(z=0,t)=0$), it naturally results in the annihilation/cancellation of vertical magnetic fields of opposite sign. This diffusion therefore reproduces the observational properties of CME-prolific decaying solar active regions (Démoulin et al. 2002; van Driel-Gesztelyi et al. 2003; Schmieder et al. 2008).

We have chosen a photospheric resistivity $\eta^{\rm phot} = 3\,\eta \sim 1.44 \times 10^{-3}$. Thus, the photospheric diffusion occurs faster than the coronal one, and slower than the shearing motions (prescribed in Sect.2.3). The associated characteristic diffusion time scale for the vertical magnetic fields is $t_\eta^{\rm phot} = (K^2\,\eta^{\rm phot})^{-1} \sim 280\ t_A$, calculated by using $K \sim 2\pi/H$ for the wavenumber of the magnetic field configuration perpendicular to the PIL, for which the relevant horizontal length scale $H = 2L = 4$ is twice the

distance between the center of the two polarities. Using Eq. (8), the evolution of $B_z(z=0)$ can be calculated in two dimensions, independently of the coronal evolution. By $t = 110\ t_A$, this results in a $\approx 10\%$ drop of the magnetic flux, due to flux cancellation at the PIL, and a decrease of the vertical field maxima by $\approx 25\%$ (resp. 50%) in the negative (resp. positive) polarity.

Our method of modeling flux cancellation in the line-tied photosphere differs from previous approaches (see e.g. van Ballegooijen & Martens 1989; Forbes & Isenberg 1991; Amari et al. 2000). But it is of the same form which Amari et al. (2003b) and Mackay & van Ballegooijen (2006) applied at their photospheric boundary, except that they only diffused the vertical component of the magnetic fields, due to their use of a staggered mesh in which the horizontal components of the magnetic field are not prescribed at the same layer.

Even though the modeled photospheric magnetic fields evolve like those of decaying active regions, our method (and the ones to which it is similar) does not necessarily contain the physics of flux dispersal in the photosphere. Firstly, magnetic field decay in active regions is a result of the random walk and possible reconnection of magnetic flux concentrations around convective cells. This is not necessarily equivalent to magnetic diffusion. Secondly, the drop in resistivity by a factor of 3 between $z = 0$ and $z = d = 6 \times 10^{-3}$ generates spurious finite $\nabla \cdot \mathbf{B}$ above the boundary (since no $\nabla\eta$ term was included in the induction equation). Fortunately, they do not generate large errors in the simulation (owing to the small rate at which $\nabla \cdot \mathbf{B}$ increases, as compared to that at which it is diffused by the resistivity). Also, since all MHD equations are written in their fully developed form in our code, i.e. with all $\nabla \cdot \mathbf{B}$ terms being removed, these small errors do not cause unphysical induction or acceleration. The same behavior is found in other MHD codes, which include so-called "Powell terms" as source terms on the right-hand side of the equations written in the conservative form.

2.3. *Photospheric shearing motions*

In addition to the photospheric diffusion, we prescribe a time-dependent horizontal boundary velocity $\mathbf{u}_\perp(z = 0; t)$. It is defined by:

$$\mathbf{u}_\perp(z=0;t) = \gamma(t)\,\mathbf{u}_\circ(t) \tag{10}$$

$$\mathbf{u}_\circ(t) = u_\circ^{\max}\,\psi_0(t)\ \left[\,\nabla_\perp\,\psi(t)\,\right] \times \mathbf{e}_z \tag{11}$$

$$\psi(t) = \exp\left[-\psi_1\left(\frac{B_z(z=0;t)}{B_z^{\min}(z=0;t)}\right)^2\right]. \tag{12}$$

There, $\mathbf{e}_z$ is the unit vector along the z axis. We set $\psi_1 = 3.5$, $u_\circ^{\max} = 0.05$, and we choose the ramp function $\gamma(t)$ as in Eq. (9). The latter results initially in infintesimal shearing velocities, which then increase and stay nearly constant for $t > 15\ t_A$. $\psi_0(t)$ is changed at each time step, such that the maximum value of $\psi_0(t)\,\nabla_\perp\,\psi(t) \times \mathbf{e}_z$ is always 1. The maximum shearing velocity is then $|\mathbf{u}_\perp(z=0;t)| = 0.05 = 5\%\ c_A(t=0)$. Since the velocities follow isocontours of $B_z(z=0;t)$, the shape of the flow changes in time, according to the diffusion-driven evolution of $B_z(z=0)$.

At all times during our simulation, the photospheric flows consist of two asymmetric, incompressible ($\nabla_\perp \cdot \mathbf{u}_\perp = 0$), clockwise-rotating, and annular-shaped vortices (see Fig. 1). Their shapes vary slowly in time, but remain qualitatively the same throughout the simulation. The vortices are centered around the maxima of $|B_z(z=0;t)|$ in the magnetic polarities, but their annulus shape results in not twisting the strong vertical field regions. So unlike in other models where round-shaped vortices twist the central parts of flux concentrations (Amari et al. 1996b; Török & Kliem 2003; Aulanier et al. 2005a), the field line bundles that are rooted in the strong field regions here do not expand due to twist injection, so their downward magnetic tension can confine field lines located below them. The vortices are rather of the same type as used by Amari et al. (2003a), but here they are asymmetric and more circular, so they do not lead to a local quasi-2.5D geometry around the PIL. Since the vortex velocities follow isocontours of the vertical magnetic field, i.e. $(\mathbf{u}_\perp \cdot \nabla_\perp)B_z = 0$, and since the vortices are incompressible, the vertical magnetic field in the photospheric plane $z = 0$ evolves merely through the effect of diffusion (see Eq. [8]).

Fig. 1 shows the amplitudes $u_\circ(t=0)$ in the annular-shaped vortices, as well as the evolution of magnetic field lines between $t = 0$ and $25\ t_A$. It shows in particular that the asymmetry of the magnetic field configuration is such that the vortices are not magnetically connected to each other by coronal field lines, except near the PIL. This "non-mapping" of the vortices into one another progressively amplifies the assymmetry of the magnetic field along the PIL (see Sect. 4.2), which is not present in most MHD simulations of shearing, twisting and erupting bipoles mentioned above. The effect of the photospheric magnetic field diffusion is visible by the changing shapes of the isocontours for the vertical magnetic field. Since the velocity magnitudes depend only on the horizontal gradients of B_z, and since the magnetic configuration is defined by the sum of two submerged monopoles that are close to one another (see Sect. 2.1), the fastest motions occur close to the PIL, leading there to the largest accummulation of magnetic shear and electric currents. Around the PIL, the shearing motions are of a few percents of $c_A(t=0)$, the maximum value $5\%c_A(t=0)$ occurring only at one point within the positive polarity. Field lines rooted in vortex areas farthest from the PIL are also sheared (in the opposite sense than those close to the PIL), but since the imposed velocities are small in these areas, and since these field lines are relatively long, their shearing does not yield strong electric currents.

We do not claim that our line-tied evolution necessarily corresponds to a realistic solar evolution. First, large and coherent shearing and twisting motions are not frequently observed on the Sun (although see Brown et al. 2003; Roudier et al. 2008, for some observations). Second, photospheric motions may not be able to induce a very large magnetic shear in the corona, due to significant departures from line-tying in the photosphere (as discussed in Grappin et al. 2008). Nevertheless, we choose this method because it ensures that magnetic shear develops mostly around the PIL of the photospheric bipole, while outer arcades remain close to potential (e.g. Schmieder et al. 1996; Schrijver et al. 2008).

2.4. *Dimensionalizing the model to solar active regions*

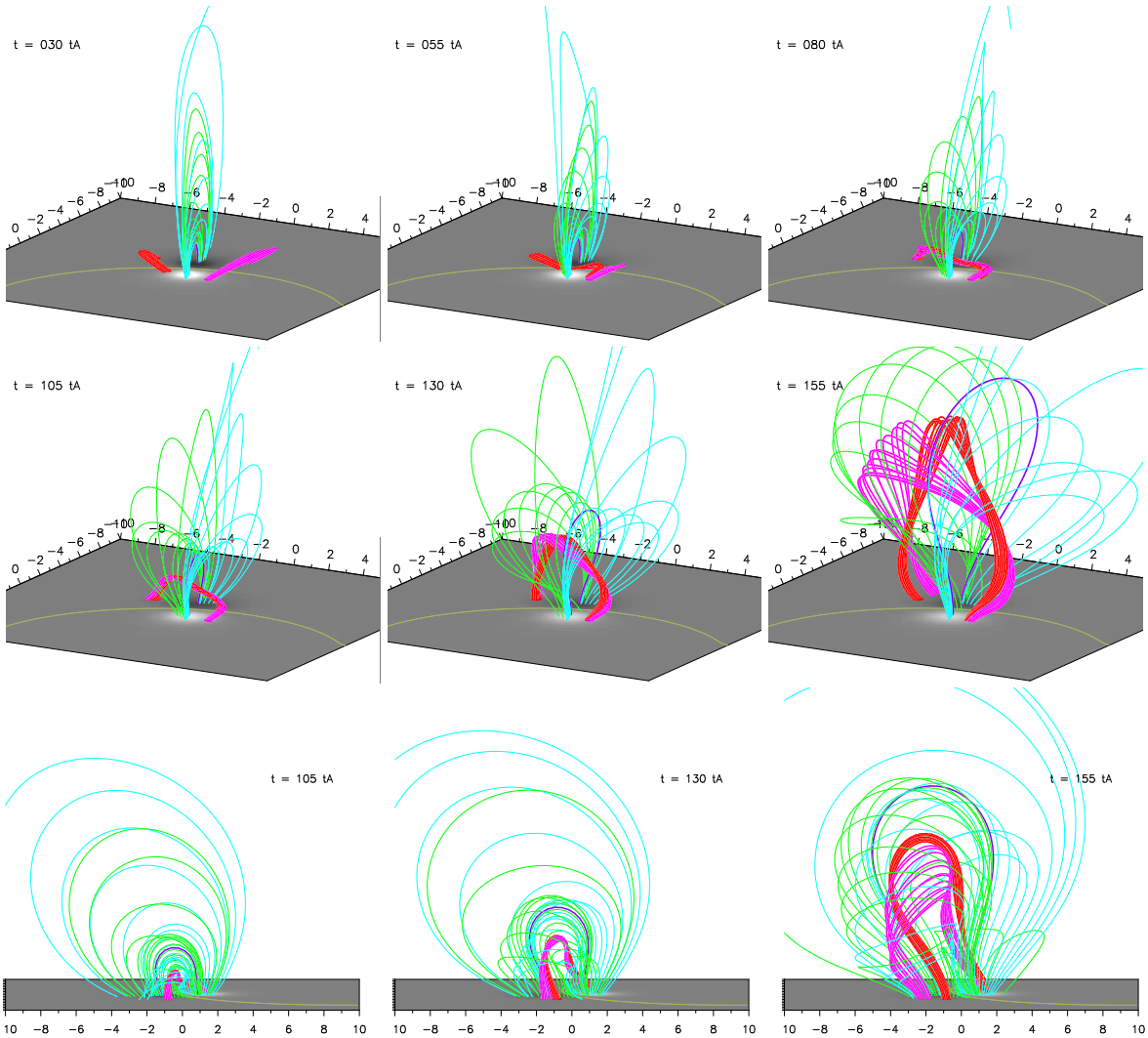

FIG. 2.— Magnetic field evolution of the shearing and diffusing bipole, before and during the eruption. The greyscale indicates $B_z(z=0)$, light/dark gray standing for positive/negative values. The yellow curve shows the polarity inversion line (PIL) $B_z(z=0)=0$. Pink/cyan field lines are drawn from the same footpoint positions $(x,y,z=0)$ in the weak/strong magnetic fields in the positive polarity at $z=0$. Red/green field lines and the dark blue one are drawn from the same footpoint positions in the weak/strong magnetic fields in the negative polarity at $z=0$. Both footpoints of the dark blue line are rooted close to the center of the annular vortices (where the velocity is negligible). Pink/red field lines belong to a forming and erupting weakly twisted flux rope, and cyan/green (resp. blue) field lines belong to moderately sheared (resp. unsheared) overlying arcades. The *top* and *middle* rows show three-dimensional projection views *[they are available as an mpeg animation in the electronic version of this paper]*. The *bottom row* shows a nearly two-dimensional projection view along the flux rope axis (i.e. y direction).

Our calculations are achieved in a dimensionless form (the magnetic permeability is set to $\mu=1$). The extrema of the vertical magnetic fields at $B_z(z=0)$ are $-B_\circ=-6.93$ and $2.45\ B_\circ$ in the negative and positive polarity, respectively. The magnetic fluxes through the photospheric plane, $\int\int|B_z(z=0;t=0)|dxdy$, are $F_\circ=37.3$ and $1.23\ F_\circ$ in the negative and positive polarity, respectively (their ratio does not match that of C_2/C_1, as defined by Eq. [5], because of the subphotospheric connection between the sources). The initial magnetic energy $E_m(t=0)$ is $E_\circ=166$.

By dimensionalizing the simulation with physical values typical solar active regions, i.e. $L=60$ Mm, $B_\circ=500$ G, and $c_A(t=0)=1000$ km/s, we obtain $F_\circ=2.4\times10^{22}$ Mx for the magnetic flux of the negative polarity, $E_\circ=1.9\times10^{33}$ erg for the magnetic energy of the potential field, $u_\circ^{\max}=50$ km/s for the maximum horizontal velocity in the photosphere, and $t_A=30$ s for the Alfvén time. The applied photospheric velocities are much faster than observed ones, but still very sub-Alfvénic, which puts them in the right physical regime of the corona. During the simulation, the photospheric shearing motions generate the induction of strong horizontal fields as well as the dilution of the plasma density. Both contribute in increasing the Alfvén speed by a factor $\sim 2-5$ at low altitudes within the highly stressed fields in the corona.

3. FLUX ROPE BUILD-UP PHASE

In this section, the pre-eruptive energy storage phase of the magnetic field configuration is described. A corresponding view of the evolution of representative field lines in the whole numerical domain is shown in the top row of Fig. 2.

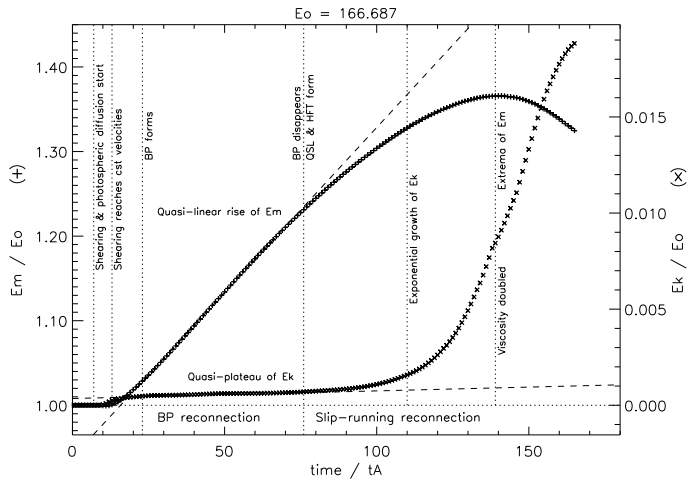

FIG. 3.— Evolution of magnetic (E_m) and kinetic (E_k) energy, normalized by the magnetic energy of the initial potential field ($E_\circ$), and plotted with + and × symbols, respectively. Key periods of the system's evolution (as annotated) are separated by vertical dotted lines.

3.1. *Flux rope formation through flux cancellation*

During the long build-up phase of the system, the kinetic energy remains roughly constant, showing some very weak oscillations, and the magnetic energy increases quasi-linearly, as shown in Fig. 3. The velocities do not grow above a few percents of $c_A[t=0]$, so the magnetic field evolves quasi-statically.

At early times ($t \lesssim 22\ t_A$), the photospheric diffusion has no noticable effect, and the magnetic field evolves solely in response to the slow shearing motions (Fig. 1). Due to the resulting increase of magnetic pressure, the initially flat sheared field lines which are located close to the PIL slowly bulge upward ($u_z < 0.01 c_A[t=0]$) and develop an "inverse tear drop" shape when seen along the PIL. As a result, the horizontal field component perpendicular to the PIL changes from negative to positive values at the footpoints of these field lines, which permits the photospheric diffusion to modify the topology from that of a simple sheared arcade to that of a 3D bald patch (BP), just as in 2.5D flux cancellation models (Forbes & Isenberg 1991; van Ballegooijen & Martens 1989), and in 3D models which used very elongated magnetic polarities (Amari et al. 2003b; Mackay & van Ballegooijen 2006).

BPs are characterized by $(\mathbf{B}_\perp \cdot \nabla_\perp) B_z > 0$ along the PIL, at which $B_z = 0$. Magnetic field lines are therefore concave upward and tangential to the photosphere along a BP. In our simulation, the BP appears at $t = 23\ t_A$, first at one point at the PIL, close to $(x;y) = (0;0)$, where the shear is strongest. Due to the combined effects of flux cancellation at the PIL and of the shearing motions, it grows linearly in size until $t = 70\ t_A$ (to a length comparable to half of the distance between the two photospheric polarities), before it shrinks and finally disappears at $t = 76\ t_A$ (see below). The left panels of Fig. 4 show the three-dimensional shape of the BP separatrix (yellow and green field lines), close to the time at which the BP is the longest along the PIL. This separatrix is composed of two joint curved surfaces, the photospheric footprints of which display an S-shaped pattern. The field lines rooted at the ends of the BP (in red and pink in Fig. 4) are J-shaped as viewed from above. For $t = [23-75]\ t_A$, the topology of the magnetic field is therefore the same as described in Titov & Démoulin (1999).

Once the BP separatrix has formed, electric currents quasi-spontaneously develop along it. A current sheet forms due to the differential displacements of the field lines in the corona, which is induced by the photospheric shearing motions on both sides of the BP separatrix (as explained in Low & Wolfson 1988). Fig. 4 shows a vertical cut of the currents across the separatrix. There, the currents display a U-shaped pattern, with their maxmimum being located at the BP. This is consistent with other MHD simulations of current sheet formation within BP separatrices (Pariat et al. 2009). We note that the current sheet forms in our simulation long before the eruption occurs. It is therefore not a by-product of the eruption.

Magnetic field lines reconnect at the BP during its whole life time. This BP reconnection abruptly changes the connectivity of the sheared field lines which pass through the growing BP separatrix, as exemplary visible in the top panels of Fig. 2: the red and pink field lines reconnect at the BP (between $t \approx [50-75]\ t_A$), yielding new field lines which are typically twice as long. This "photospheric tether-cutting" effect of the BP reconnection leads to a sudden, short-lasting ($t \approx [23-25]\ t_A$) vertical acceleration of the sheared field lines (and in turn of the overlying arcade) at the onset of the BP reconnection. However, it does not yield any eruption. The vertical coronal velocities remain approximately constant ($u_z \approx 0.015\ c_A[t=0]$), until $t \sim 80\ t_A$, when standard coronal tether-cutting reconnection sets in (see Sect. 3.2), since the tension force of the overlying arcade field lines confines the sheared field lines at low altitudes (as discussed in Sect. 2.3). Rather, the BP reconnection in our simulation progressively builds a weakly twisted coronal flux rope of less than 2π twist, which is anchored in the photosphere at both ends, surrounded by the hooks of the S-shaped BP separatrix plotted in Fig. 4. We note that the BP reconnection does not accelerate plasma jets, since it occurs right at the photospheric boundary. This is probably an artifact of our treatment of flux cancellation, which is presumably present also in the other models cited above.

Analytical arguments (Aly & Amari 1997) predict that a shearing BP separatrix eventually bifurcates into two intersecting separatrices, which for 2D configurations intersect at an X-point. Such a bifurcation indeed occurs in our 3D simulation, but forming a quasi-separatrix layer (QSL) rather than an X-point, as briefly described in Sect. 3.2. As a result, the BP eventually shrinks within less than ten Alfvén times, until it completely disappears at $t = 76\ t_A$. At this time, 6% of the vertical magnetic flux has been cancelled by the photospheric diffusion (Fig. 5), and 80% of this cancelled flux has been added to the axial flux of the flux rope.

3.2. *Tether-cutting slip-running reconnection*

Before its disappearance, the BP separatrix footprint at $z = 0$ has an asymmetric S-shape. Its hook at $(x;y) > 0$ has a smaller curvature radius than the one at $(x;y) < 0$ (see the left panels of Fig. 4). This asymmetry is a simple consequence of the smaller magnetic flux density in the negative polarity. When the BP fully

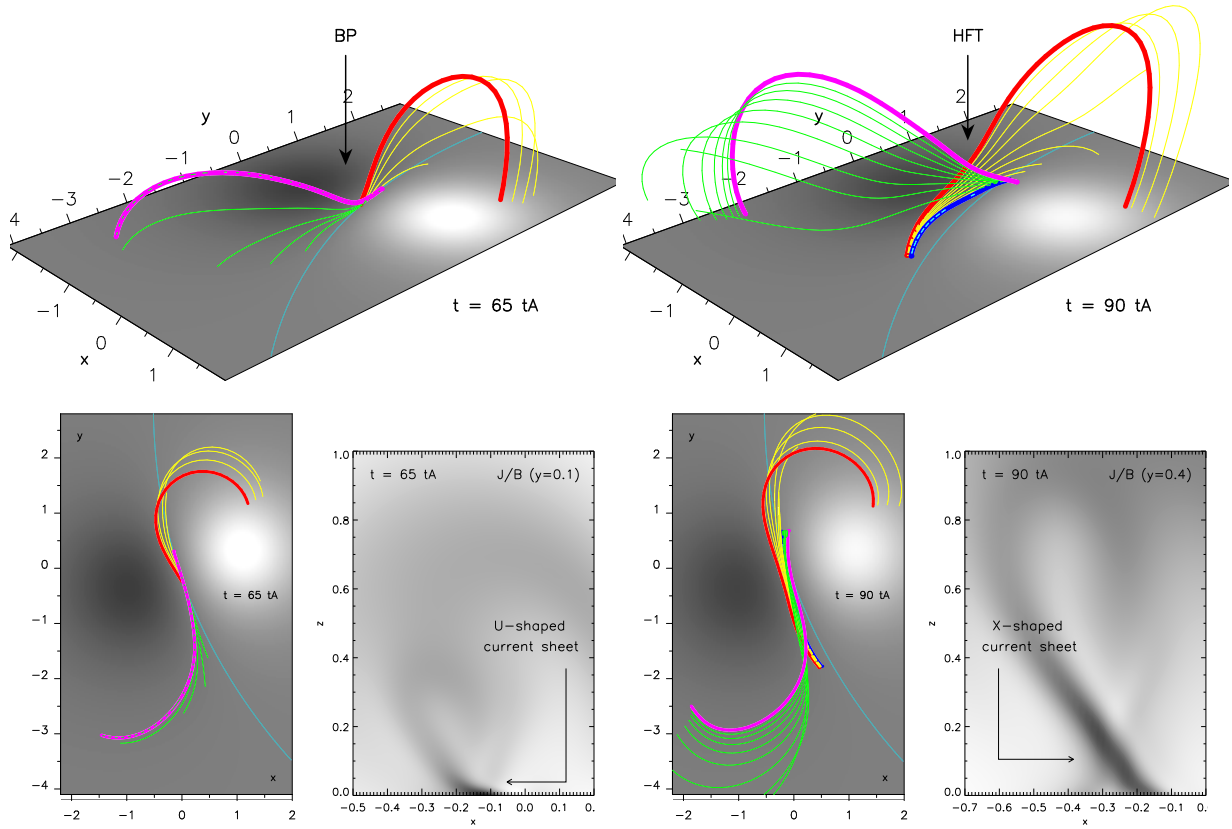

FIG. 4.— Evolution of the magnetic field topology at two different times during the energy build-up phase of the system. The colored panels show projection and top views of selected field lines, which pass through a photospheric bald patch (BP, indicated by an arrow) at $t = 65\ t_A$, and through a hyperbolic flux tube (HFT, indicated by an arrow) at $t = 90\ t_A$, which has formed after the BP has disappeared (see text for details). In these panels, the greyscale plane indicates $B_z(z = 0)$, light/dark gray standing for positive/negative values, and the cyan line is the photospheric inversion line $B_z(z = 0) = 0$. At $t = 65\ t_A$ (resp. $90\ t_A$), the field lines are integrated from footpoints at z=0 along the BP (resp. across narrow current layers that correspond to QSL footpoints). In the projection views, a vertical stretching by a factor 2 was applied to obtain a better visibility of the field line geometry. In the bottom panels, the two greyscale images show a negative rendering of vertical cuts of the electric currents normalized to the magnetic field j/B. At $t = 65\ t_A$ (resp. $90\ t_A$) the U-shaped (resp. X-shaped) current pattern corresponds to the BP (resp. the HFT).

disappears at $t = 76\ t_A$, its whole separatrix turns into one narrow QSL, which is a narrow volume across which magnetic field lines have strong connectivity gradients (see e.g. Démoulin et al. 1996; Titov et al. 2002; Aulanier et al. 2005b).

The QSL displays two J-shaped footprints at $z = 0$, which initially perfectly match the hooks of the previous BP separatrix, and which later expand as more and more magnetic flux reconnects through the QSL. Representative QSL field lines are plotted in Fig. 4, at 14 Alfvèn times after the BP has disappeared, which allows to better see the low-lying sheared (blue) field lines that cross the PIL above the location of the previous BP. The field lines plotted in Fig. 4 indeed trace a QSL, since the distance between their footpoints far from the PIL is much larger than the short segment located close to the PIL, along which their initial footpoints are anchored. These field lines display a double J-shaped pattern, and they surround the twisted flux rope. Such flux rope related QSLs have first been identified in non force-free (Démoulin et al. 1996), as well as in force-free (Titov 2007) flux rope models, and more recently in MHD simulations of erupting flux ropes (Kliem et al. 2004).

The topological transition from an S-shaped BP separatrix, to a double J-shaped QSL also occurs when force-free flux ropes rigidly emerge through a reference boundary (Titov 1999, 2007). The mechanism at the origin of this topological transition in our simulation will be described in a future paper. The associated photospheric current layer also bifurcates from a full S-shape into two J-shaped patterns, whose footprints are visibile in Fig. 6. In the simulation, these QSL-related currents are weaker than those which develop in the strong field regions of the bipole. This is due to the relatively weaker B in the QSLs than in the middle of the flux concentrations. In the latter, the currents j are extended, whereas in the former they form thin layers in which j/B is maximum. In the QSLs, we expect j to be even larger for higher grid resolutions.

A coronal hyperbolic flux tube (HFT, see Titov et al. 2002) exists within the core of our flux rope related QSL, just as in the model of Titov (2007). The HFT is the generalization of a 2.5D X-point or a 3D separator. The middle part of the HFT is located above the photospheric plane, where the red/yellow and pink/green systems of field lines converge around the blue arcade. The electric currents display a 2D X-shaped pattern around the HFT (see the right panels of Fig. 4). This is the same as what was found in Aulanier et al. (2005b) for HFTs being due to a complex distribution of the photospheric magnetic field, instead of being due to the presence of a coronal flux rope. At $t \approx 100\ t_A$, the electric cur-

rents within the HFT start to develop in an elongated (vertical) layer (as in Aulanier et al. 2005b), in which three-dimensional finite-B reconnection (as opposed to null point reconnection) takes place. In the HFT, this naturally results in slipping and slip-running reconnection, which manifest as sub- and super-Alfvénic field line slipping motions, respectively (as identified in Aulanier et al. 2006, 2007). Slip-running reconnection starts from $t = 76\ t_A$, when the HFT forms. However, the rate at which field lines reconnect through the HFT, as well as the norm of the current density within it significantly increase at $t \approx 100\ t_A$, once the vertical current layer has developed.

Just as in BP reconnection, slip-running reconnection converts J-shaped field lines (e.g. red and pink field lines plotted in the right panels of Fig. 4) into longer S-shaped field lines, which feed the previously formed flux rope with new magnetic flux. Since it occurs in the corona, this reconnection forms also small sheared arcades below the flux rope (see the blue field line at $t = 90\ t_A$ in Fig. 4, or the yellow and orange ones at $t = 145\ t_A$ in Fig. 6). These can be related to flare loops, which typically form both under activating sigmoids and in the wake of CMEs (e.g. Manoharan et al. 1996). This reconnection therefore corresponds to the standard tether-cutting reconnection, occuring in the corona. Owing to the QSL-related finite and sharp gradients in the connectivity of the sheared magnetic field lines that run parallel to the PIL, we argue that 3D tether-cutting reconnection that takes place in the corona (as proposed by Sturrock 1989; Moore & Roumeliotis 1992; Moore et al. 2001) must always occur in a slipping or/and slip-running regime.

After the bifurcation of the BP into the QSL, the time-derivative of the magnetic energy $\partial E_m/\partial t$ decreases (Fig. 3). At the same time, the kinetic energy leaves its plateau and slowly increases, and the vertical expansion of the system becomes faster (Fig. 5), even though it does not lead to an eruption yet. We have checked that the configuration is stable by performing relaxation simulations at different times $t \leq 110\ t_A$, resetting $u_\circ^{\max} = \eta^{\rm phot} = 0$. This shows that, even though tether-cutting reconnection can help feeding a flux rope from the flux of its surrounding sheared arcade, it does not lead to its eruption. Still, our simulation at later times shows that the pre-eruptive tether-cutting slip-running reconnection is exactly of the same nature as the flare reconnection that takes place below the CME, even though it occurs at a higher rate than during the pre-eruptive phase.

The relation between QSL and slip-running tether-cutting reconnection, before and during the eruption, will be analyzed in our forthcoming paper.

4. FLUX ROPE ERUPTION

In this section, the energy release phase that corresponds to the eruption of the previously formed magnetic flux rope is described. The evolution of representative field lines is shown in the middle and bottom rows of Fig. 2.

4.1. *Eruption dynamics*

From about $t \approx 100\ t_A$, the system gradually enters a phase of fast expansion, during which both the flux rope and the overlying arcade field lines accelarate to heights much larger than the size of the bipole (Fig. 2). Energetic signatures of the beginning eruption become also visible around this time (Fig. 3): the kinetic energy gradually enters a phase of exponential rise, and the time derivative of the magnetic energy starts to diminish at a faster rate. The decrease of magnetic energy by the field expansion and by magnetic reconnection eventually overcomes its increase caused by the shearing motions, and the magnetic energy starts to decrease at $t = 138\ t_A$. The energy curves shown in Fig. 3 are very similar to those obtained by Lynch et al. (2008) for their 3D breakout model.

We quantify the upward expansion of the system by the evolution of the apex of the field line rooted in the centers of the annular vortices (shown in dark blue in Fig. 2). This field line is not affected by the shearing motions, and can hence easily be followed in time. Also, it can correspond to the front of the CME, which is the feature which is commonly tracked in coronographic observations. Its rise behavior is very similar to both the flux rope and to

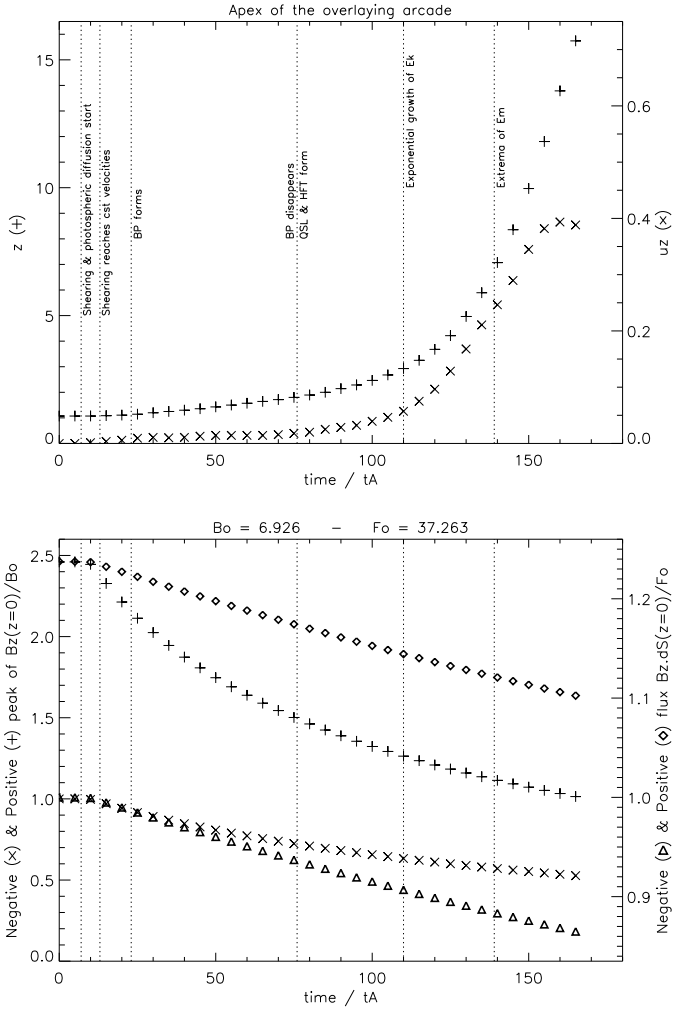

FIG. 5.— [*top:*] Evolution of the altitude z (+ signs) and the vertical velocity u_z (× signs) of the apex of the same blue field line as shown in Fig. 2. This field line is located above the forming and erupting flux rope. The time periods indicated by dotted lines are the same as in Fig. 3. [*bottom:*] Evolution of the maxima of $|B_z(z=0)|$ (shown by × and + signs), and of the magnetic fluxes $\int\int |B_z(z=0)|\ dxdy$ through the photosphere (shown by △ and ◇ signs), for both the negative (× and △) and positive (+ and ◇) polarity.

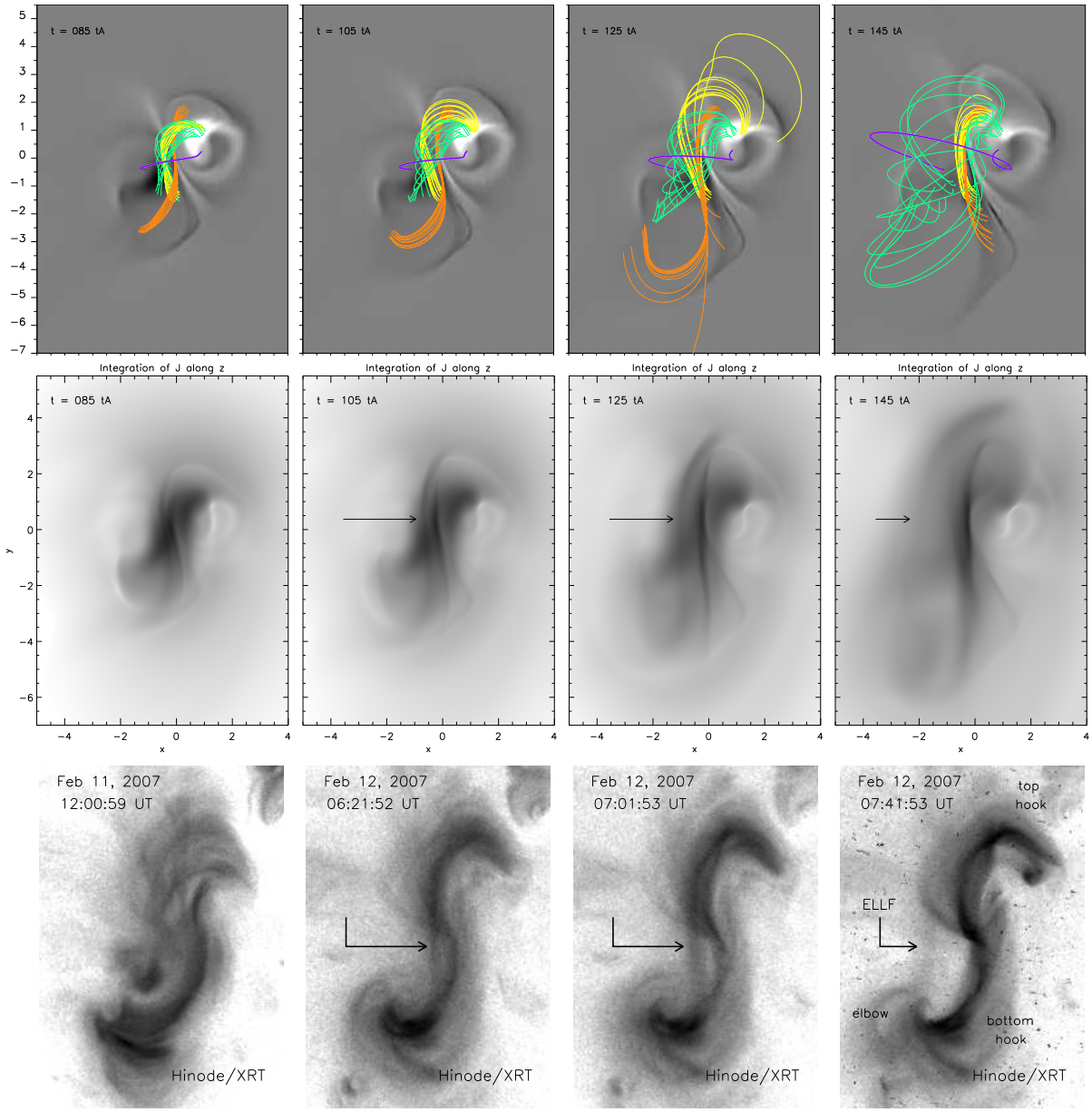

FIG. 6.— [*top:*] The greyscale indicates $j_z(z=0)$, dark/light greys standing for negative/positive values. The orange/green field lines have fixed footpoint positions in the weak/strong magnetic fields in the positive polarity at $z=0$. The yellow field lines, and the same dark blue one as in Fig. 3, have fixed footpoint positions in the weak/strong magnetic fields in the negative polarity at $z=0$. Orange/yellow field lines form a double-J pattern in the pre-eruptive stage, and turn into sheared flare loops during the eruption through slip-running reconnection. [*middle:*] Negative greyscale rendering of $\int j(z)\,dz$, emulating pre-eruptive and eruptive features in solar sigmoids as observed in soft X-rays. Darker grey indicates more intense currents. Note the thinning and dimming of the sigmoid ends, the brightening of the sigmoid axis, and the detachment of an eruptive loop-like feature (ELLF; see text for details) from the sigmoid center, marked by arrows starting at fixed positions. [*bottom:*] *XRT* observations of the 2007 February 12 erupting sigmoid (which have been rotated by 142 degrees clockwise) with an inverse grey-scale where dark (resp. light) grey areas show bright (resp. faint) soft X-ray emissions. The soft X-ray ELLF is marked by arrows. *[the top and middle rows are available as two mpeg animations in the electronic version of this paper].*

other overlying arcade field lines. Figure 5 shows that, after the slow rise phase during the pre-eruptive evolution, the apex velocity quickly increases to $\approx 0.1\ c_A(t=0)$ for $t=100-120\ t_A$, then further increases (almost linearly), until it saturates at $\approx 0.4\ c_A(t=0)$ (about 20 times the average photospheric shear velocity) at $t\approx 155\ t_A$. By $t=165\ t_A$, the apex has reached $z\approx 16$, which is ≈ 4.6 (≈ 15) times its altitude at $t\approx 120\ t_A$ ($t=0$). If we dimensionalize the simulation as in Sect. 2.4, these values correspond to a velocity of 400 km/s and to a height of $0.7\ R_\odot$ above the solar surface.

The large velocity increase during the eruption triggers numerical instabilities, which develop at large z and which halt the simulation at $t=142\ t_A$. This problem was solved by restarting the calculation from $t=138\ t_A$ with a twice as large viscosity ν', which did not seem to have a significant effect on the dynamics of the system (see Figs. 3 and 5).

We have checked that the eruption is not driven by the footpoint motions, by performing two relaxation calculations (see Sect. 3.2), starting from $t=120$ and $125\ t_A$. These relaxations result in very similar dynamics, with

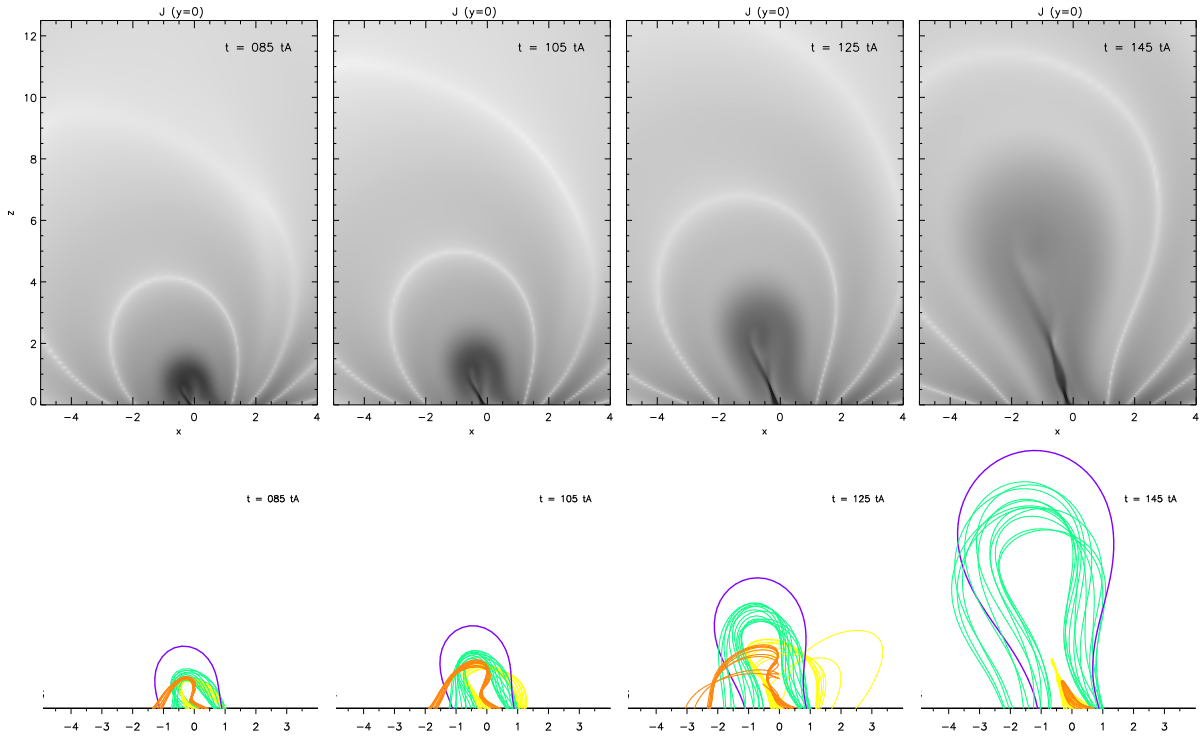

FIG. 7.— [*top:*] Negative greyscale rendering of a cut of the electric currents j at $y = 0$. Darker grey indicates more intense current. The white curves show magnetic surfaces along which $j = 0$, which separate the regions of positive and negative $j \cdot \mathbf{b}$. [*bottom:*] Two-dimensional projection along y of the same field lines as drawn in Fig. 6.

the magnetic energy naturally decreasing right from the beginning of the relaxations.

Once the system has sufficiently expanded, both the arcade field lines overlying the flux rope (Figs. 2 and 7) and the coronal electric current densities (Fig. 7) display a wide inverse tear drop shape, when seen along the y direction. Such a shape is typical for CMEs observed above the solar limb. In the simulation, it outlines the sum of two distinct electric current systems. The first one is a growing arc of relatively weak and extended currents that is generated by the footpoint motions, within the sheared field lines that overlie the flux rope (shown in green in Figs. 6 and 7). These extended electric currents are nearly aligned with the magnetic field, and they do not form along QSLs. In the model, this CME-like tear drop shape, manifested by a horizontal expansion which is smaller at lower than at larger heights, is a natural consequence of the relatively lower magnetic pressure surrounding the flux rope at large heights. The model therefore states that the legs of CMEs do not strongly expand horizontally, and that the overall CME shape is not that of a "cone model" as sometimes used for observational analyses.

The second current system is a relatively strong and narrow current system that starts to develop at the BP surface, around the forming flux rope at $t \approx 30\ t_A$, and which develops an oval shape after $t \approx 50\ t_A$ (see Fig. 4). As this oval rises in altitude and tends to detach from the photospheric plane, a small current layer develops beneath it, and starts to stretch vertically, at $t \approx 85\ t_A$, with a rate that increases during the eruption (see Fig. 7). This evolution corresponds to the transformation of the BP separatrix into an HFT (see Sect. 3.2), with the vertical layer forming within the HFT (as in Török et al. 2004).

4.2. *Asymmetric eruption*

The asymmetry of the initial potential field (Sect. 2.1) results in asymmetries of the erupting magnetic field.

A first asymmetry occurs in the direction of the PIL. The middle row in Fig. 2 shows that the part of the flux rope (pink and red field lines) located above $y < 0$ rises faster than the one located above $y > 0$. Fig. 6 shows that this behavior is also evident in the overlying arcades (green field lines). It results from the asymmetric build-up of the pre-eruptive flux rope. The asymmetry of the shearing motions, combined with the BP reconnection, result in a sheared/twisted flux tube whose center is offset in negative y direction from the center of the bipole (see Figs. 2 and 4). Since the magnetic field strength, and hence the restraining tension of the overlying arcade, decreases with distance from the bipole center, the part of the flux rope above $y < 0$ expands faster than the rest of the rope. Such a variation of the magnetic tension of the overlying arcade along the PIL may be the origin of "zipping-like" prominence eruptions (Lyot 1937; Tripathi et al. 2006; Liu et al. 2009), in which one end of a prominence (or filament) starts to rise before the other end.

A second asymmetry of the eruption occurs in the direction perpendicular to the PIL (see bottom panels in Fig. 2). It is caused by the flux imbalance of the bipole (see Sect. 2.4), which increases in time as a result of the flux cancellation, from 23% at $t = 0$, to 27% at $t = 110\ t_A$ (Fig. 5, bottom panel). This imbalance is the cause for the existence of a wide area within the positive polarity, from which field lines leave the domain through the open boundaries, hence resembling "open" field lines, as

in solar coronal holes. This imbalance results in a negative magnetic pressure gradient along x, which prevents the flux rope to expand in the positive x direction to the same amount as in the negative x direction. This asymmetry matches the observed non-radial rise of erupting filaments and CMEs (e.g. Williams et al. 2005), as well as the observed CMEs deflection from radial trajectories, caused e.g. by coronal holes located on one side of the CME (Subramanian et al. 1999; Delannée et al. 2000; Schmieder et al. 2000).

4.3. *Evidence for the torus instability*

From the energetics and dynamics of the system (Sect. 4.1) and from the relaxation runs (Sects. 3.2 and 4.1) one can deduce that the eruption is triggered between $t = 110$ and 120 t_A. This shows that the onset of increased dynamics at $t \approx 100\ t_A$ does not correspond to the onset of the eruption. In the following, we consider $t = 120\ t_A$ as the start time of the eruption.

It is clear that the BP reconnection is not responsible for the eruption, since it takes place between $t = 23$ and $75\ t_A$, long before the eruption is triggered (see Sect. 3.1). The same can be concluded for the coronal tether-cutting reconnection, since it sets in already at $t = 75\ t_A$ and does not lead to an eruption if both the photospheric diffusion and shearing motions are stopped at any time $t \leq 110\ t_A$. Finally, even though the strongest photospheric magnetic fields significantly decrease due to the imposed photospheric diffusion, the disappearance of total magnetic flux through cancellation at the PIL is not very large during the whole simulation, being of the order of 10% at the time when the eruption starts (Sect. 2.2 and Fig. 5, bottom). This relatively small drop is unlikely to diminish the energy of the open field below the energy of the system at the start of the eruption; a condition which appears to be necessary for an eruption to be driven by flux disappearance (according to Amari et al. 2000). We therefore argue that neither bald patch reconnection, nor tether-cutting reconnection, nor flux disappearance are responsible for the eruption in our model. Nevertheless, all three effects contribute in building a flux rope from sheared arcades and to slowly lift it up in altitude.

On one hand, the pre-eruptive acceleration of the magnetic fields between $t = 100$ and 120 t_A is an indication that the system behaves as predicted by the non-equilibrium circuit models (see Sect. 1.2). It strongly resembles the behavior of a line current which approaches the critical point $(h_c; I_c)$ of the equilibrium curve $h(I)$, as driven by a constant increase of I. Close to the critical point, $\partial h/\partial I$ gradually increases, so that a linear increase of $I(t)$ must lead to an upward acceleration of the line current. But on the other hand, this behavior could also be consistent with the simple existence of a steep equilibrium curve with no critical point (e.g. Aulanier et al. 2005a). We therefore test if either the cartesian (van Tend & Kuperus 1978) or the axisymmetric (Bateman 1978; Kliem & Török 2006) condition for non-equilibrium is satisfied in our fully 3D line-tied simulation.

To do so, we first have to identify the location of the flux rope axis at the time of the eruption. This is important for making the analogy with a circuit model, since the rope axis would there correspond to the line current around which the magnetic field is twisted. At $t = 120\ t_A$, the fastest vertical expansion of the magnetic field within our asymmetric flux rope takes place above $(x_a = -0.25; y_a = -0.9)$. This gives the x and y positions of the flux rope apex at the onset of eruption. In the right panel of Fig. 8 we plot $B_x(x_a, y_a, z)$ at various times. The increasing separation of the curves there confirms the start of the eruption at $t = 120\ t_A$ as derived from the relaxation runs. Since the rope is twisted, and since its central part runs nearly parallel to the y axis at the times represented in Fig. 8, the altitude of the rope axis $z_{\rm axis}$ must be located where $B_x(x_a, y_a, z)$ changes sign from > 0 to < 0 with increasing z. Note that, except for $t \approx 120\ t_A$, this altitude yields only an approximate height of the axis apex, since the flux rope does not ascend vertically (see Sect. 4.2). At the onset of the eruption at $t = 120\ t_A$, Fig. 8 shows that $z_{\rm axis} = 1.9$.

Next we have to obtain the external magnetic field, which provides the restaining tension on the flux rope, and hence corresponds to the external potential field in the circuit models. Since this field cannot be easily separated from the field created by the flux rope current itself, we approximate it by the potential field $\mathbf{B}_{\rm pot}$ that corresponds to the vertical photospheric magnetic field at $t = 120\ t_A$ (as done by Fan & Gibson 2007). This potential field is calculated using the FFT method (Alissandrakis 1981), with 2048×2048 Fourier modes in the $(x; y)$ horizontal directions, using a horizontal box which size is 250×250, in which the boundary condition is $B_z(z = 0) = B_z(z = 0; t = 120\ t_A)$ in $(x; y) \in [-10, 10]$ and $B_z(z = 0) = 0$ elsewhere. This very large box size, more than two order of magnitude larger than L, was used to minimize the aliasing effects which are intrinsic to this FFT method.

We then calculate $n(z) = -\partial \ln B_{\rm pot}(x_a, y_a, z)/\partial \ln z$, which is a local measure of the magnetic field drop-off along the z axis (see Török & Kliem 2007). Due to the asymmetry of the initial magnetic field configuration (see Sect. 2.1), all three components of $\mathbf{B}_{\rm pot}$ are $\neq 0$ along (x_a, y_a, z) for all z, in contrast to the circuit models, for which the external field is purely perpendicular to the current. Therefore, we calculate $n(z)$ not just for the total field $B_{\rm pot}$, but also for its horizontal part $B_{{\rm pot};\perp} = (B^2_{{\rm pot};x} + B^2_{{\rm pot};y})^{1/2}$. These two field profiles are plotted in the left panel of Fig. 8. Their corresponding $n(z)$ are plotted in the insert of this panel. The resulting field profiles are nearly indistinguishable between $z = 1$ and 3. Note that $n(z)$ for $B_{{\rm pot};x}$ and $B_{{\rm pot};\perp}$ are almost exactly superposed to one another for all z. The critical heights at which the external field starts to drop faster than z^{-1} and $z^{-3/2}$, are $z^{\rm c}_1 = 1.2$ and $z^{\rm c}_{3/2} = 2$, respectively.

In summary, when the eruption starts, at $t = 120\ t_A$, the apex of the axial field line of the flux rope has reached the altitude $z_{\rm axis} = 1.9$, which is very close to the critical altitude $z^{\rm c}_{3/2} = 2$ for the onset of torus instability, as estimated from the potential component of the magnetic field. So our analysis strongly suggests that the flux rope eruption can be described in terms of the loss of stability of a toroidal current, which has previously developed during a long energy storage phase, and which has eventually reached the altitude at which the magnetic field decreases sufficiently fast with height above the photosphere for the torus instability to develop (Bateman 1978; Kliem & Török 2006).

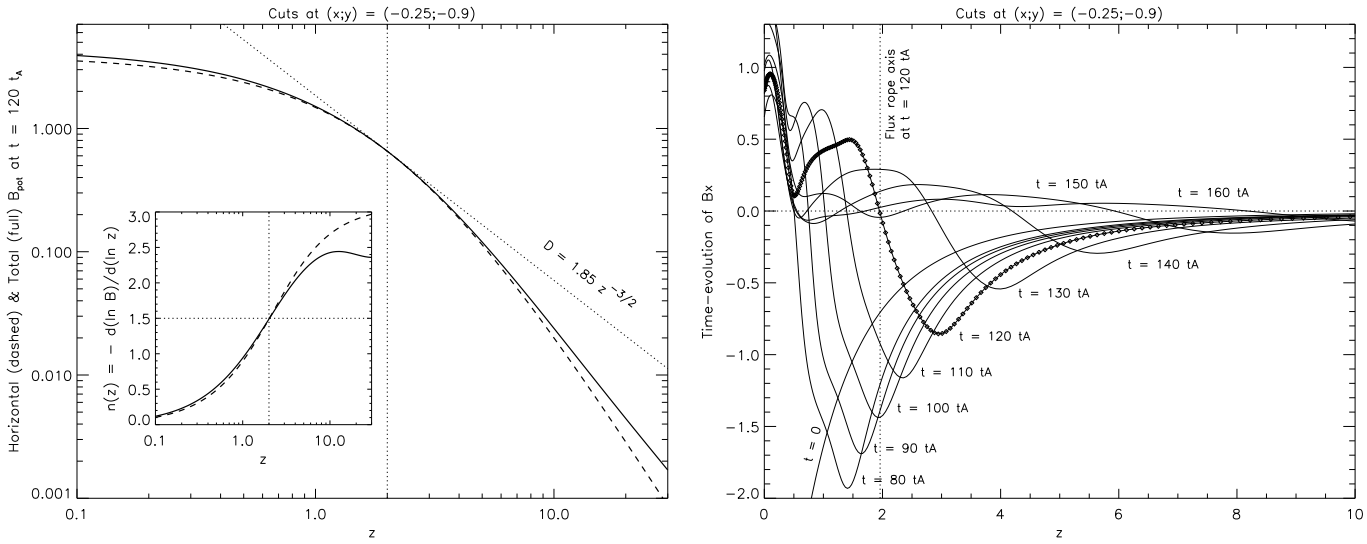

FIG. 8.— [*left:*] Vertical dependence of the norm of the total (solid line) and horizontal (dashed line) potential magnetic field $B_{\rm pot}$ (extrapolated from $B_z(z=0;t=120t_A)$), at the $(x;y)$ position that corresponds to the fastest magnetic field expansion during the eruption. The altitude $z=2$ above which the magnetic fields drop faster than $z^{-3/2}$ is indicated by the vertical dotted line. The insert shows the vertical dependence of the decay index $n(z)=-\partial \ln B_{\rm pot}/\partial \ln z$ (see text for details). [*right:*] Evolution of $B_x(z)$ at the same $(x;y)$ position as in the left panel. The diamonds at $t=120\ t_A$ indicate the position of grid points along z. The altitude $z=1.9$ of the flux rope axis at which $B_x=0$ at $t=120\ t_A$ is indicated by a vertical dotted line.

4.4. *Remarks*

In this Section, we discuss four issues raised by our identification of the torus instability as the driver of the eruption is our flux cancellation model.

First, it is noteworthy that this critical height is slightly larger that the one obtained by considering the initial potential field $B(x_a;y_a;z;t=0)$: the latter gives $z^{\rm c}_{3/2}=1.85$ instead of 2. On the one hand the increase of $z^{\rm c}_{3/2}$ in time between $t=0$ and 120 t_A shows that the effect of flux dispersal in the photosphere (that results from the magnetic diffusion), actually acts against, and not in favor of, the onset of the torus instability, since it puts its threshold to larger and larger heights. On the other hand this effect is not very large, since the increase of $z^{\rm c}_{3/2}$ is of $\approx 8\%$ only. To be conservative, we argue that in the flux dispersal and cancellation model, an eruption can eventually be triggered by the torus instability only if the slow rise in altitude of the flux rope during the pre-eruptive phase occurs at a faster rate than that of the critical height, the latter being directly related to the rate of dispersal for photospheric magnetic flux.

Second, even though our simulation finds a strong CME acceleration by the time the current-carrying flux rope has developed a semi circular shape, its physics greatly differ from that of the circuit model of Chen & Krall (2003), which also predicts a similar behavior. Indeed, the latter is not a storage-and-release model. This family of circuit models requires a dynamic injection of significant poloidal flux around the flux rope to drive its eruption (Forbes et al. 2006), whereas our relaxation runs (Sects. 3.2 and 4.1) indicate the existence of stable equilibria for $t\leq 110\ t_A$ and free eruptions for $t\geq 120\ t_A$.

Third, our simulation cannot be conclusive regarding the following theoretical question: is the torus instability triggered when the flux rope just enters an unstable branch of the equilibrium curve, or is it triggered when the rope just passes an unstable critical point where a stable and unstable branch of the equilibrium curve meet, beyond which no equilibrium would exist? In other words, is the eruption a manifestation of an instability, or of a catastrophic loss of equilibrium? Even though the initial torus instability theory has been developed for unstable equilibria (Bateman 1978; Kliem & Török 2006), the possible existence of associated critical points has been proposed by Isenberg & Forbes (2007), so a catastrophe scenario cannot be ruled out.

Fourth, we do not disregard the possibilty that in other configurations, initially flat and slowly rising flux ropes might erupt before developing a semi-circular shape and reaching a height at which the decay index of the external field becomes $\approx 3/2$. Such eruptions are suggested by the cartesian circuit model, which contains a straight line current and predicts $n(z)=1$. In our simulation, the total flux rope current might be simply too small, or not sufficiently twisted for this particular loss of equilibrium to occur while the rope is still flat. We leave this question to a future study.

5. DECONSTRUCTING OBSERVATIONS OF SIGMOID ERUPTIONS

5.1. *Case study of the 2007 February 12 event*

In this section, we use simplified soft X-ray signatures of our simulation to interpret the eruption of a sigmoid, which was observed by the *X-Ray Telescope* (*XRT*, see Golub et al. 2007) onboard the *Hinode* satellite (Kosugi et al. 2007) on 2007 February 12, around 7:00 UT. *XRT* images of the sigmoid around the time of its eruption are shown in Fig. 9. This event was analyzed by McKenzie & Canfield (2008), modeled by non-linear force-free fields by Savcheva & van Ballegooijen (2009), and compared to a flux emergence model by Archontis et al. (2009).

The photospheric vertical magnetic field associated with the sigmoid is composed of a single bipolar decaying active region (see the SOHO/MDI magnetograms in McKenzie & Canfield 2008; Savcheva & van Ballegooijen 2009), which is consistent with our flux cancellation sim-

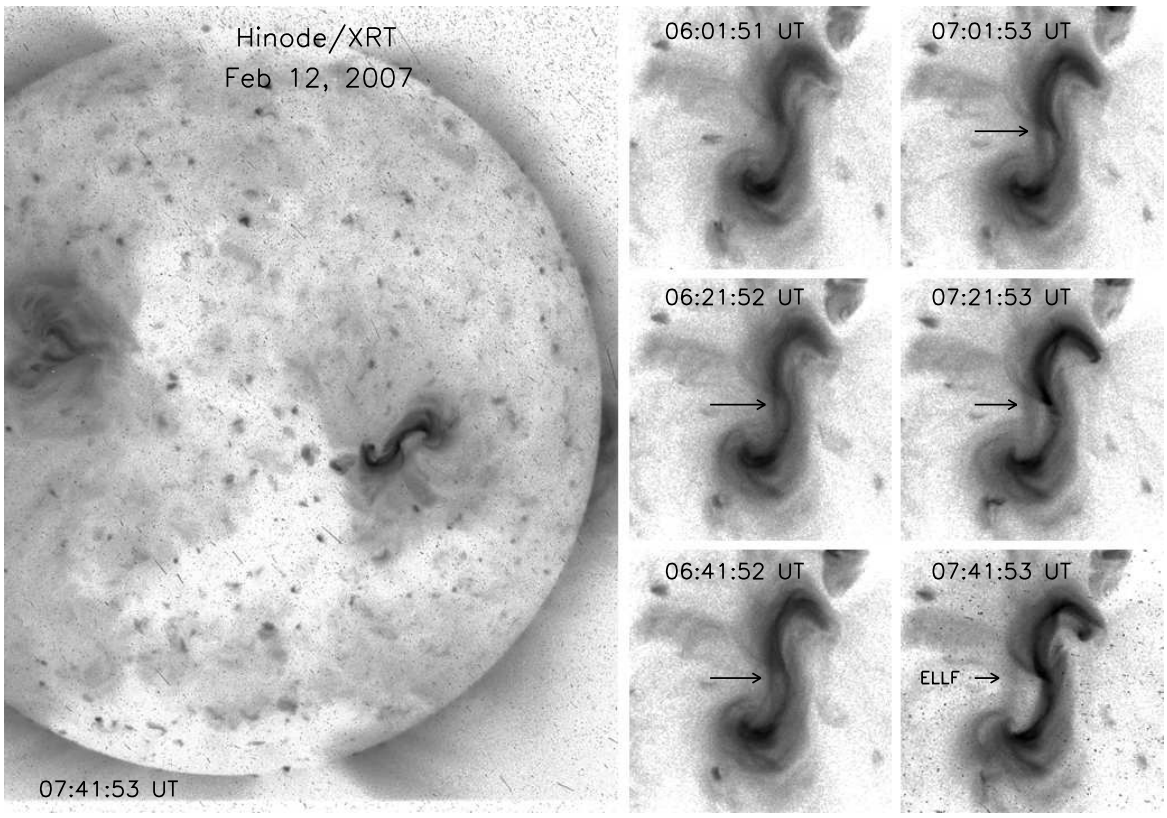

FIG. 9.— *XRT* observations of the 2007 February 12 erupting sigmoid, with an inverse grey-scale where darker (resp. lighter) areas show brighter (resp. fainter) soft X-ray emissions. The six panels on the right have been rotated by 142 degrees clockwise, i.e. solar North is toward the bottom-right of these images. The arrows indicate the central part of the ELLF.

ulation. Note that for comparison with our model, we rotated the *XRT* observations by 142° clockwise (see the right panels of Fig. 9 and the bottom row of Fig. 6). In the following, we refer to the eastern (western) part of the sigmoid as its top (bottom) part, respectively.

The comparison of our fully 3D asymmetric eruption model with the observations yields new interpretations of various observed features in this particular sigmoid. Based on past observations of other erupting sigmoids, we argue that these interpretations probably apply to most soft X-ray sigmoids.

5.2. *Slip-running reconnection in J-shaped loops*

The studied sigmoid is not a transient feature that brightens only during its eruption. *XRT* observations show its presence from at least February 10, 11:00 UT (McKenzie & Canfield 2008). However, at this time it is not yet composed of an ensemble of long S-shaped coronal loops, but it is rather formed by the alignment of numerous J-shaped loops (see the bottom left panel in Fig. 6). Note that the sigmoid is asymmetric, as its top loops are shorther than its bottom loops. During a time period of $\approx$ 24 h before the eruption, several transient thin, fully bright S-shaped loops in the middle of the sigmoid are visible, each lasting $\approx 0.5 - 1$ h. Only after $\approx$19:00 UT on February 11, persistent fully S-shaped loops can be observed.

The long-lasting double-J pattern led McKenzie & Canfield (2008) to suggest that the sigmoid emissions are due to steady heating within a bald patch separatrix (hereafter BPS) surrounding a flux rope (as in model of Titov & Démoulin 1999). The existence of many threads within each J has been reproduced in the high-resolution flux emergence simulation by Archontis et al. (2009). The double-J pattern was there formed at the location of a BPS in the early stage of the emergence, and the occurrence of multiple threads within the sigmoid was associated with reconnection at numerous small-scale current layers within the main double-J pattern, which developed during the emergence.

In our simulation, a double-J ensemble of field line bundles forms right before the onset of the BP reconnection, due to the shearing of the magnetic field. These field lines reconnect at the BP, and later on at the HFT (see Sect. 3), and should therefore be heated and be filled with hot plasma, i.e. become visible in soft X-ray emission. Examples of such field lines are plotted in red and pink in Fig. 4, as well as in yellow and orange in Figs. 6 and 7 from $t = 85\ t_A$, shortly after the BPS has bifurcated into a QSL (see Sect. 3.2). The middle row in Fig. 6 shows an integration of the current density along the z direction in our simulation. We use this quantity as a simple proxy for the expected soft X-ray emission (see Sect. 5.3 for detailed discussion).

Both field line and integrated current plots show a relatively good match between the simulated sigmoid and the one observed by *XRT* on 2007 February 11. Different information can be grasped from both types of plots (see below), so that none is sufficient to understand to observations when considered alone. The different sizes of the two Js are reproduced. Our synthetic sigmoid significantly grows in size during the simulation. This is due to the continuing shearing motions, which yield re-

connecting field lines of progressively increasing length (see top views in Figs. 4 and 6). During the energy build-up phase, the vertically integrated current maps show a striking resemblance to observations of forming sigmoids (see e.g. the Fig. 2 of Green & Kliem 2009). During the eruption phase, we regard our not observed continuing growth of the sigmoid as an artifact of our model, which is probably caused by unrealistically fast photospheric diffusion and motions (as compared to solar values), applied to an initially unsheared bipolar field (whereas many solar active regions are already far from being potential when they form).

We find that some magnetic loops rooted in the bottom J, that have one end which passes below (and farther from) the top J along the PIL, are found both in the model and in the observations (see the orange lines which pass below the yellow lines at $t = 85 - 105\ t_A$, and the faint loop between the two Js on February 11, at 12:00:59 UT (see Fig. 6). This "cross-over" of J-shaped field lines only occurs after the disappearance of the BPS in our simulation.

These J-shape field lines eventually endure tether-cutting reconnection (see Sect. 3.2 and 4.1). Two new stable field lines form, once their fast slippage resulting from the slip-running reconnection through the HFT (as in Aulanier et al. 2006) has ended: one long S-shaped loop, and one lower lying shrinking sheared field line which is of the flare loop type (see the bottom rows of Figs. 2 and 7). The amount of flux that reconnects at the HFT gradually increases from $t = 85\ t_A$ up to the time of the eruption. This is consistent with the gradual pre-eruptive formation and brightening of S-shaped loops between February 11, 19:00 UT and February 12, 6:00 UT, as well as with the sudden brightening of the sigmoid during the eruption between 6:00 UT and 8:00 UT on February 12 (see McKenzie & Canfield 2008; Archontis et al. 2009, and Figs. 6 and 9).

In summary, our simulation suggests that the observed sigmoid is formed by pairs of J-shaped field lines, which can indeed be heated through photospheric BP reconnection as proposed by McKenzie & Canfield (2008), but which can also be heated through coronal tether-cutting slip-running reconnection at later times, resulting in their merging into full S-shaped loops and in the formation of small flare loops below the sigmoid. We argue that the later process can account for the evolution of many observed sigmoids before they erupt (Manoharan et al. 1996; Rust & Kumar 1996; Sterling & Hudson 1997; Sterling et al. 2000; Gibson et al. 2002).

5.3. *Extended and QSL currents in thinning sigmoid hooks*

The sigmoid eruption on 2007 February 12 shows in its later phase the formation of round-shaped twin dimmings (often referred to as "transient coronal holes") (see also Manoharan et al. 1996; Sterling & Hudson 1997; Sterling et al. 2000; Hudson et al. 1998). Before the occurrence of these dimmings, the sigmoid ends (which we refer to as "hooks" hereafter) progressively thin. This thinning is best visible in the top hook between 07:01 and 07:41 UT, but also in the bottom hook between 07:21 and 07:41 UT (see Figs. 6 and 9). In retrospective, we find that such thinning of sigmoid hooks in the early stages of their eruption is also visible in previously studied events observed by *Yohkoh/SXT* and *GOES/SXI*, see e.g. Fig. 2 c,d in Manoharan et al. (1996), Fig. 2 a,b in Sterling et al. (2000), and Fig. 4 in Moore et al. (2001), as well as Fig. 2 (last column) in Liu et al. (2007).

On one hand, the thinning of sigmoid hooks might simply correspond to the first stages of the formation of the dimmings. On the other hand, the difference in shape between dimmings and hooks may imply a different mechanism. Our MHD simulation provides a possible interpretation for the thinning of sigmoid hooks in the early stage of their eruption that is not based on a drop in plasma density.

Our interpretation relies on a very simplified ad-hoc modeling of the soft X-ray emission, presuming that the emission is proportional to the line-of-sight integration of the Joule heating term ηj^2 obtained in the simulation. For simplicity, we assume that the direction of integration is along z, and in order to allow the simultaneous visualization of both bright and faint features, we integrate the square root of the Joule heating term, $\int j(z)\ dz$.

A similar approach was used in other sigmoid (Aulanier et al. 2005a; Magara 2006; Archontis et al. 2009) and sheared active region (Schrijver et al. 2008; DeRosa et al. 2009) models. We do not claim that the real soft X-ray emissivity is given by this quantity. It is well known that the X-ray brightening of individual flux tubes also occurs as a natural consequence of the increase of their plasma density, following some heating episode. Nevertheless, we argue that there must be also a monotonic contribution of the electric current density in the soft X-ray emissivity in sigmoids, since sigmoids are observable only in very hot EUV lines and in soft X-rays, which indicates that they are hotter than the surrounding corona, while at the same time they are associated to large-scale sheared or twisted flux tubes, which indicates that their field-aligned currents are larger than those in the surrounding corona.

Figure 6 shows that $\int j(z)\ dz$ displays a sigmoidal shape long before the eruption starts, just like the magnetic field lines do. The regions of strongest $\int j(z)\ dz$ are located above the PIL. At their locations, the photospheric currents are small, which confirms that the central part of the modeled sigmoid is located at coronal heights (as in Aulanier et al. 2005a; Schrijver et al. 2008). The sigmoid hooks are more complex: from the field line point of view, they are associated with the ends of highly sheared field lines; from the electric current point of view, they are formed by two distinct current systems, which evolve differently as explained in the following.

First, extended regions of strong $\int j(z)\ dz$ are present in the inner parts of the sigmoid hooks, located above the regions where strong $B_z(z = 0)$ and $j_z(z = 0)$ coincide. Before the eruption, these low altitude currents increase as the magnetic shear increases. Owing to the asymmetric, sub-Alfvénic annular vortices, magnetic shear develops close to the middle of the positive polarity, even though the shearing motions are zero there. This apparent contradiction can be explained as follows. Let us consider the blue field lines shown in Fig. 1. Since they are rooted in the vortex within the negative polarity, and since the motions are both slow and line-tied, nearly force-free electric currents j naturally develop all along them. This implies the generation of $j \simeq \lambda \mathbf{B}$, with λ being nearly constant along a given field line. This

means that electric currents can be generated at $z = 0$, along the arc-shaped ensemble of footpoints of these blue field lines. This initially arc-shaped current layer eventually develops a spiral pattern as the field line footpoints move within the positive polarity (as explained in Aulanier et al. 2005a). During the eruption, these low-altitude currents decrease quickly as a direct consequence of the expansion, since it reduces the magnetic twist per unit length, which is proportional to the current density (see Klimchuk & Sturrock 1989; Aulanier et al. 2005a).

Second, thin loop-like threads of $\int j(z)\ dz$ are also present along the modeled sigmoid (see Fig. 6), both before and during the eruption. Two of these threads have C shapes, and each of them constitutes the outer edge of one hook. They perfectly match with the photospheric current layers, which are visible as narrow $j_z(z = 0)$ layers in the top row of Fig. 6 and which are formed within the QSLs (see Sect. 3.2). The related currents slowly increase as a function of time, due to the decrease of the scale lengths of the magnetic gradients (which are of the order of $\mathbf{B}/\nabla \times \mathbf{B}$) within the vertical current layer (which are shown in Fig. 7). These scale lenghts decrease during the dynamic pinching of the HFT caused by the fast expansion of the flux rope above it (see Sect. 4.1)

In summary, assuming that the quantity $\int j(z)\ dz$ is a monotonic proxy for the softX-ray emissions observable in sigmoids, our model predicts that the extended inner parts of sigmoid hooks should dim during the eruption, as a result of current decrease driven by the expansion, whereas the thin outer edges of the hooks should brighten as a result of the collapse of the flare-related vertical current layer. This behavior perfectly matches the *XRT* observations of the 2007 February 12 event (see Fig. 6), as well as those of previously studied erupting sigmoids.

5.4. *Deploying coronal currents in the erupting loop-like feature*

An elongated feature that detaches from the center of the sigmoid around 06:21 UT is visible during the 2007 February 12 eruption (McKenzie & Canfield 2008). It accelerates toward the south-west (i.e. toward the left in Fig. 6), while it progressively faints until it becomes invisible after 07:41 UT. Due to its narrow shape, we call it an "erupting loop-like feature" (hereafter ELLF). This ELLF is visible only in five *XRT* frames, which are shown in Fig. 9. Such ELLFs have already been reported from past *Yohkoh/SXT* sigmoid observations (see, e.g., the features labelled with D in Figs. 3 - 6 of Moore et al. 2001) and have been generally associated with an erupting flux rope (Moore et al. 2001; McKenzie & Canfield 2008).

Based on the $\approx$ 9 degree clockwise rotation of the ELLF axis, and the forward S shape of the sigmoid, McKenzie & Canfield (2008) suggested that the flux rope might have erupted due to a kink instability (e.g. Fan & Gibson 2004; Török & Kliem 2005; Williams et al. 2005; Green et al. 2007). The frames of Fig. 9 (which are less saturated than the corresponding ones shown in Fig. 4 of McKenzie & Canfield 2008) highlight that the bottom part of the ELLF seems to curve in the same way as the nearby sigmoid hook. This ELLF "elbow" is slightly offset from the outer edge of the sigmoid hook (see the bottom right panel in Fig. 6). The apparent continuous connection between the straight part and the elbow of the ELLF is best visible at 06:41 UT. In the kinking flux rope interpretation, this elbow would correspond to one of the flux rope ends.

Figure 6 shows that the our $\int j(z)\ dz$ proxy for the soft X-ray intensity (see Sect. 5.3) readily reproduces the shape and the dynamics of the ELLF, including its rotation and its curved elbow, even though the modeled flux rope does not become kink-unstable during the whole simulation. Hereafter we analyse the relation between the magnetic field lines and electric currents in our model, and we provide a new interpretation for this puzzling ELLF.

Figures 6 and 7 indicate that the straight central part of the modeled ELLF is not part of the erupting flux rope, but a signature of the tear-drop-shaped extended current layers that overlie the flux rope. The figures show that this "current shell" is located within the green field lines, which are rooted in the positive polarity (see below), and within the strong electric currents, which first amplify and later diminish in the inner parts of the thinning sigmoid hook (see Sect. 5.3). The currents within the straight part of the ELLF are volumetric and decrease during the field line expansion, which shows that this feature does not form within a QSL. In our model, the straight part of the ELLF is actually orthogonal to the local magnetic fields. The detachment of the modeled ELLF from the sigmoid center is a consequence of the non-radial, asymmetric eruption of the magnetic field perpendicular to the PIL. It is best visible above the negative photospheric magnetic flux concentration (see Fig. 6).

In order to confirm the association of the green field lines shown in Figs. 6 and 7 with the ELLF, we consider in Fig. 10 the shape of the vertical currents $j_z(z = 4.5)$ at $t = 150\ t_A$, as well as the field lines which pass through these regions of intense currents. At this time, the ELLF pattern has clearly detached from the modeled sigmoid. The altitude $z = 4.5$ was chosen because it corresponds to the middle section of the region where the current shell is mainly vertical on the left-hand side of the sigmoid, so where the currents give the strongest contribution to $\int j(z)\ dz$ and therefore to the modeled ELLF. Note that $z = 4.5$ is lower than the altitude of the apex of the overlying blue field line ($z = 10$; see Fig. 5), and it is comparable to the altitude of the apex of the erupting flux rope ($z = 6$; see Fig. 8). When dimensionalized to solar units (see Sect. 2.4), $z = 4.5$ corresponds to 135 Mm ($\sim 0.2\ R_\odot$) above the photosphere, which is fairly high.

The left panel of Fig. 10 shows a projection view of the currents $j_z(z = 4.5)$ and of selected field lines which pass through them. Two narrow current layers are visible. Field lines which pass through the layer which is closer (resp. farther) to the sigmoid are plotted in red/pink (resp. green/cyan). The right panels of Fig. 10 clearly confirm that the green/cyan field lines correspond to the straight part of the ELLF. These field lines are almost the same as the green lines shown in Figs. 6 and 7. The red/cyan field lines, however, clearly belong to the erupting flux rope. They are associated with the elbow of the ELLF. Figs. 6 and 10 show that both the gradual rotation of the straight part of the ELLF (reported by McKenzie & Canfield 2008) and the deformation of its elbow are a simple consequence of the asymmetry of our configura-

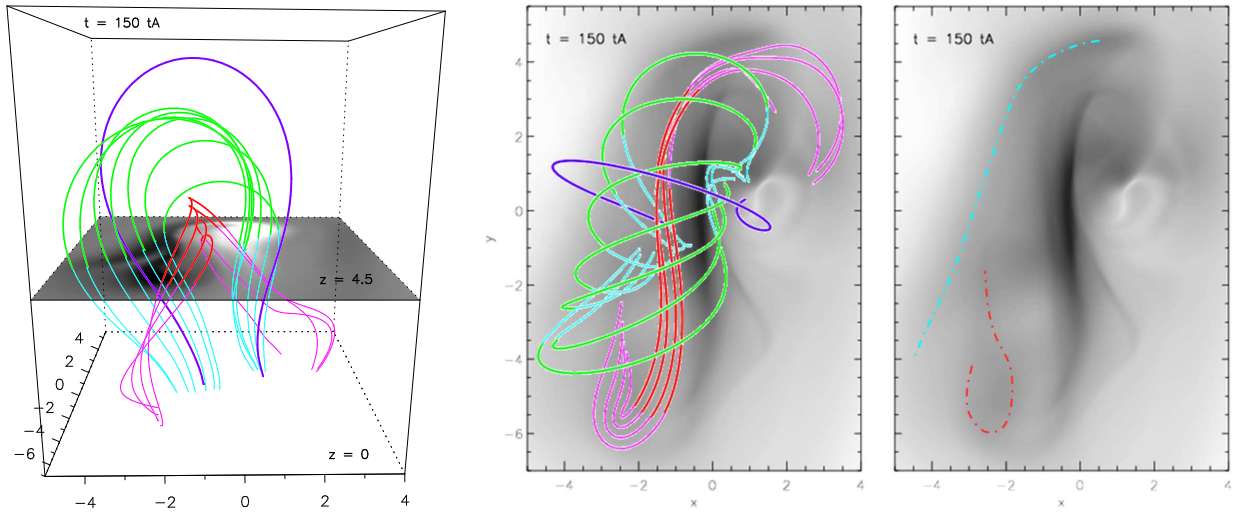

FIG. 10.— Relation between the field lines and the electric current layers deploying in the corona during the eruption at $t = 150\ t_A$. [*left:*] Projection view along the y axis (approximately along the flux rope axis). The greyscale image shows $j_z(z = 4.5)$, dark/light grey standing for positive/negative values. The height of the box is $z \in [0; 11]$. The blue field line is the same as in Figs. 2,6,7. The other field lines change color, from pink to red and from cyan to green, as they cross $z = 4.5$ within two prominent elongated current layers $j_z < 0$ located along y in $x \in [-4; -2]$. The pink/red (resp. cyan/green) field lines belong to the flux rope system drawn in red/pink in Figs. 2 (resp. to the overlying sheared arcades drawn in green in Figs. 6,7). [*middle:*] top view of the same field lines, superimposed on a greyscale image of $\int j(z)\ dz$ (as in Fig. 6). [*right:*] Image of $\int j(z)\ dz$, overlaid with two curved dashed lines. The cyan line outlines a long bar that detaches from the sigmoid and which rotates clockwise during the eruption. It corresponds to the location of the vertical portions of the cyan/green overlying arcades, and to the ELLF (see Figs. 6 and 9). The red hook shows a loop-like feature that slowly stretches during the eruption. It corresponds to the lowermost parts of the flux rope field lines.

tion (Sect. 4.2).

In summary, assuming that the quantity $\int j(z)\ dz$ can indicate the locations of soft X-ray brightenings during sigmoid eruptions, and that it can lead to observable signatures at large altitudes in the corona (in a similar way as proposed by Delannée et al. 2008, for EUV emissions), our model nicely reproduces the shape and dynamics of the weakly rotating ELLF that was observed by *XRT* on 2007 February 12, as well as the generic dynamics of previously observed ELLFs (e.g. Moore et al. 2001). The model therefore suggests that an ELLF is not a direct observational signature of an erupting flux rope, but rather of a CME-related current shell that develops within the expanding sheared arcades which overlie an erupting flux rope.

6. SUMMARY

Numerous physical effects constitute fundamental ingredients of distinct MHD models for the triggering of solar coronal mass ejections (CME). Most of them are known to take place in 3D numerical simulations of the so-called "flux-cancellation model" for CMEs, and also in other models. Moreover, circuit models predict that CMEs are driven by a loss of equilibrium of a concentrated current, which ends are most often not line-tied to the photosphere. But the non-equilibrium conditions of these circuit models are not straightforward to identify in time-dependent full MHD simulations. Indeed, coronal electric currents are not prescribed in MHD. They rather develop as a consequence of the plasma motions, which create departures from non-potentiality in line-tied magnetic fields.

In this paper, we presented a new 3D MHD numerical simulation of the flux cancellation model. In our simulation, an initially bipolar, current-free, and asymmetric coronal magnetic field evolves in response to simultaneous sub-Alfvénic annular vortex motions and to slow diffusion of the three magnetic field components, which were both prescribed at a line-tied photospheric boundary.

Our first aim was to investigate which of the distinct physical mechanisms occurring in the simulation contribute to the gradual formation and eruption of a weakly twisted flux rope. The complexity of the dynamic evolution required us to discuss the roles of topology and reconnection, but a full description of the related theory is beyond the scope of this study, and will be the object of a future paper. Our results can be summarized as follows:

- As a consequence of the imposed photospheric shear flows, magnetic field lines expand upward. Once they have bulged enough to adopt an inverse tear drop shape (as viewed in projection along the polarity inversion line, or PIL), the photospheric magnetic field diffusion changes their topology from that of sheared arcade to that of a bald patch (BP). A current sheet forms all along the resulting S-shaped bald patch separatrix (BPS). Due to magnetic reconnection occuring at the BP, individual field lines suddenly double their length, and their middle parts detach from the photosphere. A weakly twisted coronal flux rope then forms and grows both in altitude and in length. Since the BP disappears long before the flux rope erupts, the BP reconnection is merely responsible for its formation, and not for its eruption.

- The BPS later bifurcates into a QSL, which contains a hyperbolic flux tube (HFT) below the flux rope. The HFT slowly rises in altitude, and the field lines display a X-type pattern around it (as viewed in projection along the PIL). A short vertical current layer quickly forms within the HFT,

and slip-running reconnection occurs through it. This latter process is fully three-dimensional and a finite-B property of tether-cutting reconnection. During a relatively long time, this tether-cutting reconnection is not very energetic. Only shortly before the eruption, a moderate increase of the dynamics takes place, which, however, might be mainly caused by the flux rope current itself which has come close to the point of non-equilibrium. Since the tether-cutting reconnection starts long before the eruption, and since it does not significantly change the growth rate of the magnetic energy, it does not appear to drive the eruption.

- Flux dispersal due to the imposed photospheric diffusion leads to a significant and asymmetric decrease of the maximum photospheric magnetic field strength within the two polarities, of 25% and 50% respectively, up to the start of the eruption. Flux cancellation at the PIL, however, yields a relatively weak disappearance of photospheric flux of 10% only, during the same time period. This implies that the magnetic tension of the overlying arcade should still be able to confine the flux rope at the onset time of the eruption, if merely flux cancellation at the PIL would occur in the simulation. Photospheric flux cancellation alone is therefore unlikely to produce the eruption of the flux rope.

- The flux rope eruption starts when the highest part of its axial field line reaches the altitude z above which the decay index of the overlying magnetic field becomes $n = -\partial \ln B/\partial \ln z \gtrsim 3/2$. At this time, the flux rope has developed a nearly semi-circular shape. Both conditions are in accordance with the onset criteria of the "torus instability", which can drive the free radial expansion of an electric current ring in axisymmetric circuit models. This instability occurs when the decrease in altitude of the downward magnetic tension, in the external magnetic field, becomes faster than that of the upward magnetic pressure, in current-carrying magnetic fields during their rise in altitude. Our analyses lead to the conclusion that this mechanism is the actual driver of the eruption.

- In summary, we have shown that a weakly twisted flux rope forms and erupts in the flux cancellation MHD model for solar eruptions (Forbes & Isenberg 1991; Amari et al. 2003b; Mackay & van Ballegooijen 2006), even if the photospheric flux concentrations are not symmetric. The flux rope forms and rises slowly due to photospheric bald patch and coronal slip-running tether-cutting reconnection, which both do not trigger its eruption. The flux rope finally erupts as a result of the development of the torus instability in its highest portion (Kliem & Török 2006; Isenberg & Forbes 2007). Our simulation qualitatively reproduced the distinct rise phases typically observed in CMEs, and allowed us to attribute distinct physical mechanisms to each of these phases.

In the second part of the paper, we modeled observational signatures for soft X-ray sigmoids in our simulation. These signatures are based firstly on the structure of magnetic field lines that have already reconnected, or that are reconnecting, and secondly on the time-evolution of deploying electric current systems, which we have proposed to be visible in soft X-rays at the zero-th order as the line-of-sight integration of the Ohmic heating term (or of its square-root). We have used these proxies for interpreting a specific event that was observed on 2007 February 12 with *Hinode/XRT* (McKenzie & Canfield 2008). This event had several features already reported in past observations of erupting sigmoids at lower resolution (e.g. Manoharan et al. 1996; Moore et al. 2001). Our physical interpretations, which are a priori not specific to one single event, are given below:

- During their pre-eruptive stages, sigmoids consist of an envelope of a double-J loop pattern. In our model, these coronal loops are J-shaped field lines, which have been heated through bald-patch reconnection during the early formation of the sigmoid. In other models, another source of heating has to be invoked for these loops to be observable. At a given time, these loops are not necessarily a trace of a BPS, but can also be located within a QSL that has a coronal HFT above the PIL. These field lines eventually merge into full S-shaped loops by a slip-running tether-cutting reconnection in the coronal HFT.

- When sigmoids erupt, the early thinning of their two hooks (before the formation of transient coronal holes) is caused by two effects. Firstly, the inner portions of the hooks dim in soft X-rays as a result of a decrease of electric currents in expanding sheared loops. Secondly, the thin outer-edges of the hooks brighten because they are formed within a QSL, the currents of which increase as a result of the thinning of the current-layer during the eruption.

- Based on the premise that layers of strong electric current correspond to soft X-ray emissions, our model suggests that the eruptive look-like feature (ELLF) that detaches from the center of erupting sigmoids does not trace the erupting flux rope, for the most part. The short and curved end of an ELLF can still be a signature of one stretching leg of the erupting flux rope. Nevertheless, the straight and longest part of the ELLF does not correspond to any magnetic loop. The straight part of the ELLF is rather the observational signature of a CME-related tear-drop shaped current-shell, which forms within the expanding sheared arcades overlying the erupting flux rope. In the absence of artificial symmetry in the system, the integration along the line-of sight of these electric currents naturally results in one narrow and straight ELLF well detached from the sigmoid. The main axis of an ELLF can weakly rotate with respect to the PIL, solely due to the differential expansion of the current-shell.

- Our interpretations for the features observed during the erupting stage of sigmoids are neither specific to the formation mechanisms of non-potential

fields in active regions (e.g. flux emergence vs. footpoint shearing), nor to the trigger mechanism of the eruption, apart from the asymmetry in the photospheric magnetic field. So, we argue that they apply to all erupting sigmoids, whatever the origin of non-potentiality in the active region and the driver of their eruption are. Indeed, the field line and electric current patterns resulting from our MHD model during the pre-eruptive energy build-up phase of the system are compatible to those obtained by Savcheva & van Ballegooijen (2009) with a non-linear force-free reconstruction of the same sigmoid to which we applied our model. It follows that further observational diagnostics and comparison between different models will be needed to better quantify the mechanisms responsible for the formation and eruption of sigmoids.

The authors thank L. Golub and the referee, for their helpful comments which improved the clarity of the paper. GA also thanks T. Amari for stimulating questions and discussions. The MHD calculations were done on the quadri-core bi-Xeon computers of the Cluster of the Service Informatique of Paris Observatory. *Hinode* is a Japanese mission developed and launched by ISAS/JAXA, with NAOJ as domestic partner and NASA and STFC (UK) as international partners. It is operated by these agencies in cooperation with ESA and the NSC (Norway). Financial supports by the European Commission through the FP6 SOLAIRE Network (MTRN-CT-2006-035484) and through the FP7 SOTERIA project (Grant Agreement n^o 218816) are gratefully acknowledged.

REFERENCES

Alissandrakis, C. E. 1981, A&A, 100, 197
Aly, J. J. 1985, A&A, 143, 19
Aly, J. J. & Amari, T. 1997, A&A, 319, 699
Amari, T. & Aly, J. J. 1990, A&A, 227, 628
Amari, T., Luciani, J. F., & Aly, J. J. 2004, ApJ, 615, L165
—. 2005, ApJ, 629, L37
Amari, T., Luciani, J. F., Aly, J. J., Mikic, Z., & Linker, J. 2003a, ApJ, 585, 1073
—. 2003b, ApJ, 595, 1231
Amari, T., Luciani, J. F., Aly, J. J., & Tagger, M. 1996a, A&A, 306, 913
—. 1996b, ApJ, 466, L39
Amari, T., Luciani, J. F., Mikic, Z., & Linker, J. 2000, ApJ, 529, L49
Antiochos, S. K., DeVore, C. R., & Klimchuk, J. A. 1999, ApJ, 510, 485
Archontis, V., Hood, A. W., Savcheva, A., Golub, L., & Deluca, E. 2009, ApJ, 691, 1276
Archontis, V., Moreno-Insertis, F., Galsgaard, K., Hood, A., & O'Shea, E. 2004, A&A, 426, 1047
Archontis, V. & Török, T. 2008, A&A, 492, L35
Aulanier, G., Démoulin, P., & Grappin, R. 2005a, A&A, 430, 1067
Aulanier, G., Golub, L., DeLuca, E. E., Cirtain, J. W., Kano, R., Lundquist, L. L., Narukage, N., Sakao, T., & Weber, M. A. 2007, Science, 318, 1588
Aulanier, G., Pariat, E., & Démoulin, P. 2005b, A&A, 444, 961
Aulanier, G., Pariat, E., Démoulin, P., & Devore, C. R. 2006, Sol. Phys., 238, 347
Bateman, G. 1978, MHD instabilities, ed. G. Bateman
Brown, D. S., Nightingale, R. W., Alexander, D., Schrijver, C. J., Metcalf, T. R., Shine, R. A., Title, A. M., & Wolfson, C. J. 2003, Sol. Phys., 216, 79
Canfield, R. C., Hudson, H. S., & McKenzie, D. E. 1999, Geophys. Res. Lett., 26, 627
Chen, J. 1989, ApJ, 338, 453
Chen, J. & Krall, J. 2003, Journal of Geophysical Research (Space Physics), 108, 1410
Chen, P. F. & Shibata, K. 2000, ApJ, 545, 524
Delannée, C., Delaboudinière, J.-P., & Lamy, P. 2000, A&A, 355, 725
Delannée, C., Török, T., Aulanier, G., & Hochedez, J.-F. 2008, Sol. Phys., 247, 123
Démoulin, P., Mandrini, C. H., van Driel-Gesztelyi, L., Thompson, B. J., Plunkett, S., Kovári, Z., Aulanier, G., & Young, A. 2002, A&A, 382, 650
Démoulin, P., Priest, E. R., & Lonie, D. P. 1996, J. Geophys. Res., 101, 7631
DeRosa, M. L., Schrijver, C. J., Barnes, G., Leka, K. D., Lites, B. W., Aschwanden, M. J., Amari, T., Canou, A., McTiernan, J. M., Régnier, S., Thalmann, J. K., Valori, G., Wheatland, M. S., Wiegelmann, T., Cheung, M. C. M., Conlon, P. A., Fuhrmann, M., Inhester, B., & Tadesse, T. 2009, ApJ, 696, 1780
DeVore, C. R. & Antiochos, S. K. 2000, ApJ, 539, 954
Emonet, T. & Moreno-Insertis, F. 1998, ApJ, 492, 804
Fan, Y. 2001, ApJ, 554, L111
Fan, Y. & Gibson, S. E. 2004, ApJ, 609, 1123
—. 2007, ApJ, 668, 1232
Filippov, B. P. & Den, O. G. 2001, J. Geophys. Res., 106, 25177
Forbes, T. G. 1990, J. Geophys. Res., 95, 11919
—. 2000, J. Geophys. Res., 105, 23153
Forbes, T. G. & Isenberg, P. A. 1991, ApJ, 373, 294
Forbes, T. G., Linker, J. A., Chen, J., Cid, C., Kóta, J., Lee, M. A., Mann, G., Mikić, Z., Potgieter, M. S., Schmidt, J. M., Siscoe, G. L., Vainio, R., Antiochos, S. K., & Riley, P. 2006, Space Science Reviews, 123, 251
Forbes, T. G. & Priest, E. R. 1995, ApJ, 446, 377
Gibson, S. E., Fletcher, L., Del Zanna, G., Pike, C. D., Mason, H. E., Mandrini, C. H., Démoulin, P., Gilbert, H., Burkepile, J., Holzer, T., Alexander, D., Liu, Y., Nitta, N., Qiu, J., Schmieder, B., & Thompson, B. J. 2002, ApJ, 574, 1021
Golub, L., Deluca, E., Austin, G., Bookbinder, J., Caldwell, D., Cheimets, P., Cirtain, J., Cosmo, M., Reid, P., Sette, A., Weber, M., Sakao, T., Kano, R., Shibasaki, K., Hara, H., Tsuneta, S., Kumagai, K., Tamura, T., Shimojo, M., McCracken, J., Carpenter, J., Haight, H., Siler, R., Wright, E., Tucker, J., Rutledge, H., Barbera, M., Peres, G., & Varisco, S. 2007, Sol. Phys., 243, 63
Grappin, R., Aulanier, G., & Pinto, R. 2008, A&A, 490, 353
Green, L. M. & Kliem, B. 2009, ApJ, 700, L83
Green, L. M., Kliem, B., Török, T., van Driel-Gesztelyi, L., & Attrill, G. D. R. 2007, Sol. Phys., 246, 365
Hudson, H. S., Lemen, J. R., St. Cyr, O. C., Sterling, A. C., & Webb, D. F. 1998, Geophys. Res. Lett., 25, 2481
Inhester, B., Birn, J., & Hesse, M. 1992, Sol. Phys., 138, 257
Isenberg, P. A. & Forbes, T. G. 2007, ApJ, 670, 1453
Isenberg, P. A., Forbes, T. G., & Démoulin, P. 1993, ApJ, 417, 368
Isobe, H., Tripathi, D., & Archontis, V. 2007, ApJ, 657, L53
Jacobs, C., Poedts, S., & van der Holst, B. 2006, A&A, 450, 793
Jacobs, C., Roussev, I. I., Lugaz, N., & Poedts, S. 2009, ApJ, 695, L171
Jouve, L. & Brun, A. S. 2009, ApJ, 701, 1300
Kim, S., Moon, Y.-J., Kim, K.-H., Kim, Y.-H., Sakurai, T., Chae, J., & Kim, K.-S. 2007, PASJ, 59, 831
Kliem, B., Titov, V. S., & Török, T. 2004, A&A, 413, L23
Kliem, B. & Török, T. 2006, Physical Review Letters, 96, 255002
Klimchuk, J. A. & Sturrock, P. A. 1989, ApJ, 345, 1034
Kosugi, T., Matsuzaki, K., Sakao, T., Shimizu, T., Sone, Y., Tachikawa, S., Hashimoto, T., Minesugi, K., Ohnishi, A., Yamada, T., Tsuneta, S., Hara, H., Ichimoto, K., Suematsu, Y., Shimojo, M., Watanabe, T., Shimada, S., Davis, J. M., Hill, L. D., Owens, J. K., Title, A. M., Culhane, J. L., Harra, L. K., Doschek, G. A., & Golub, L. 2007, Sol. Phys., 243, 3
Li, H., Schmieder, B., Aulanier, G., & Berlicki, A. 2006, Sol. Phys., 237, 85
Lin, J. & Forbes, T. G. 2000, J. Geophys. Res., 105, 2375

Lin, J., Forbes, T. G., & Isenberg, P. A. 2001, J. Geophys. Res., 106, 25053
Lin, J., Forbes, T. G., Isenberg, P. A., & Démoulin, P. 1998, ApJ, 504, 1006
Lin, J., van Ballegooijen, A. A., & Forbes, T. G. 2002, Journal of Geophysical Research (Space Physics), 107, 1438
Liu, C., Lee, J., Yurchyshyn, V., Deng, N., Cho, K.-s., Karlický, M., & Wang, H. 2007, ApJ, 669, 1372
Liu, R., Alexander, D., & Gilbert, H. R. 2009, ApJ, 691, 1079
Low, B. C. 1977, ApJ, 212, 234
Low, B. C. & Wolfson, R. 1988, ApJ, 324, 574
Lynch, B. J., Antiochos, S. K., DeVore, C. R., Luhmann, J. G., & Zurbuchen, T. H. 2008, ApJ, 683, 1192
Lyot, B. 1937, L'Astronomie, Bull. Soc. Astron. de France, 1, 203
Mackay, D. H. & van Ballegooijen, A. A. 2006, ApJ, 641, 577
MacNeice, P., Antiochos, S. K., Phillips, A., Spicer, D. S., DeVore, C. R., & Olson, K. 2004, ApJ, 614, 1028
Magara, T. 2006, ApJ, 653, 1499
Magara, T. & Longcope, D. W. 2001, ApJ, 559, L55
Manchester, IV, W., Gombosi, T., DeZeeuw, D., & Fan, Y. 2004, ApJ, 610, 588
Manoharan, P. K., van Driel-Gesztelyi, L., Pick, M., & Démoulin, P. 1996, ApJ, 468, L73
Martens, P. C. H. & Kuin, N. P. M. 1989, Sol. Phys., 122, 263
McKenzie, D. E. & Canfield, R. C. 2008, A&A, 481, L65
Mikic, Z. & Linker, J. A. 1994, ApJ, 430, 898
Molodenskii, M. M. & Filippov, B. P. 1987, Soviet Astronomy, 31, 564
Moore, R. L. & Roumeliotis, G. 1992, in Lecture Notes in Physics, Berlin Springer Verlag, Vol. 399, IAU Colloq. 133: Eruptive Solar Flares, ed. Z. Svestka, B. V. Jackson, & M. E. Machado, 69
Moore, R. L., Sterling, A. C., Hudson, H. S., & Lemen, J. R. 2001, ApJ, 552, 833
Pariat, E., Aulanier, G., Schmieder, B., Georgoulis, M. K., Rust, D. M., & Bernasconi, P. N. 2004, ApJ, 614, 1099
Pariat, E., Masson, S., & Aulanier, G. 2009, ApJ, 701, 1911
Rachmeler, L. A., DeForest, C. E., & Kankelborg, C. C. 2009, ApJ, 693, 1431
Roudier, T., Švanda, M., Meunier, N., Keil, S., Rieutord, M., Malherbe, J. M., Rondi, S., Molodij, G., Bommier, V., & Schmieder, B. 2008, A&A, 480, 255
Roumeliotis, G., Sturrock, P. A., & Antiochos, S. K. 1994, ApJ, 423, 847
Roussev, I. I., Forbes, T. G., Gombosi, T. I., Sokolov, I. V., DeZeeuw, D. L., & Birn, J. 2003, ApJ, 588, L45
Rust, D. M. & Kumar, A. 1996, ApJ, 464, L199
Savcheva, A. & van Ballegooijen, A. 2009, ApJ, 703, 1766
Schmieder, B., Bommier, V., Kitai, R., Matsumoto, T., Ishii, T. T., Hagino, M., Li, H., & Golub, L. 2008, Sol. Phys., 247, 321
Schmieder, B., Delannée, C., Yong, D. Y., Vial, J. C., & Madjarska, M. 2000, A&A, 358, 728
Schmieder, B., Démoulin, P., Aulanier, G., & Golub, L. 1996, ApJ, 467, 881
Schrijver, C. J., DeRosa, M. L., Metcalf, T., Barnes, G., Lites, B., Tarbell, T., McTiernan, J., Valori, G., Wiegelmann, T., Wheatland, M. S., Amari, T., Aulanier, G., Démoulin, P., Fuhrmann, M., Kusano, K., Régnier, S., & Thalmann, J. K. 2008, ApJ, 675, 1637
Shafranov, V. D. 1966, Reviews of Plasma Physics, 2, 103
Sterling, A. C. & Hudson, H. S. 1997, ApJ, 491, L55
Sterling, A. C., Hudson, H. S., Thompson, B. J., & Zarro, D. M. 2000, ApJ, 532, 628
Sturrock, P. A. 1989, Sol. Phys., 121, 387
Sturrock, P. A., Antiochos, S. K., & Roumeliotis, G. 1995, ApJ, 443, 804
Subramanian, P., Dere, K. P., Rich, N. B., & Howard, R. A. 1999, J. Geophys. Res., 104, 22321
Titov, V. S. 1999, in ESA Special Publication, Vol. 448, Magnetic Fields and Solar Processes, ed. A. Wilson & et al., 715
Titov, V. S. 2007, ApJ, 660, 863
Titov, V. S. & Démoulin, P. 1999, A&A, 351, 707
Titov, V. S., Hornig, G., & Démoulin, P. 2002, J. Geophys. Res., 107, A01164
Titov, V. S., Priest, E. R., & Démoulin, P. 1993, A&A, 276, 564
Török, T. & Kliem, B. 2003, A&A, 406, 1043
—. 2005, ApJ, 630, L97
—. 2007, Astronomische Nachrichten, 328, 743
Török, T., Kliem, B., & Titov, V. S. 2004, A&A, 413, L27
Tripathi, D., Isobe, H., & Mason, H. E. 2006, A&A, 453, 1111
Ugarte-Urra, I., Warren, H. P., & Winebarger, A. R. 2007, ApJ, 662, 1293
van Ballegooijen, A. A. & Martens, P. C. H. 1989, ApJ, 343, 971
van der Holst, B., Jacobs, C., & Poedts, S. 2007, ApJ, 671, L77
van Driel-Gesztelyi, L., Démoulin, P., Mandrini, C. H., Harra, L., & Klimchuk, J. A. 2003, ApJ, 586, 579
van Driel-Gesztelyi, L., Manoharan, P. K., Démoulin, P., Aulanier, G., Mandrini, C. H., Lopez-Fuentes, M., Schmieder, B., Orlando, S., Thompson, B., & Plunkett, S. 2000, Journal of Atmospheric and Solar-Terrestrial Physics, 62, 1437
van Tend, W. 1979, Sol. Phys., 61, 89
van Tend, W. & Kuperus, M. 1978, Sol. Phys., 59, 115
Vršnak, B. 2008, Annales Geophysicae, 26, 3089
Williams, D. R., Török, T., Démoulin, P., van Driel-Gesztelyi, L., & Kliem, B. 2005, ApJ, 628, L163
Yang, W. H., Sturrock, P. A., & Antiochos, S. K. 1986, ApJ, 309, 383